ABSTRACT

NANO-STRUCTURED PLATFORMS AS A SPECTROSCOPIC TOOL

by
Ruiqiong Li

Nano-structured platforms have been studied for the purpose of enhancing weak fluorescence signals. Each platform was constructed as a thin oxide layer on top of a metal (aluminum). The oxide was perforated with hexagonal array of nano-holes. The pitch of the array was much smaller than the optical wavelengths used. Surface charge waves (Surface Plasmons) could be excited when the platform was oriented at specific direction with respect to the incident optical beam. At this point one can demonstrate that fluorescence signals could be amplified. Since the oxide (alumina) is bio-compatible, one can envision using such platforms in the study of bio-species with fluorescencing bio-markers. Moreover, when imbedding dye chromophores in the structure's nano-pores, one can show that such construction exhibits threshold and gain for the related fluorescence signals.

NANO-STRUCTURED PLATFORMS AS A SPECTROSCOPIC TOOL

by
Ruiqiong Li

A Thesis
Submitted to the Faculty of
New Jersey Institute of Technology
in Partial Fulfillment of the Requirements for the Degree of
Master of Science in Electrical Engineering

Department of Electrical and Computer Engineering

January 2009

APPROVAL PAGE

NANO-STRUCTURED PLATFORMS AS A SPECTROSCOPIC TOOL

Ruiqiong Li

Dec 11, 08

Dr. Haim Grebel, Thesis Advisor — Date
Professor of Electrical and Computer Engineering, NJIT

12/10/08

Dr. Leonid Tsybeskov, Committee Member — Date
Professor of Electrical and Computer Engineering, NJIT

12/11/2008

Dr. Raquel Perez-Castillejos, Committee Member — Date
Assistant Professor of Electrical and Computer Engineering, NJIT

BIOGRAPHICAL SKETCH

Author: Ruiqiong Li

Degree: Master of Science

Date: January 2009

Undergraduate and Graduate Education:

- Master of Science in Material Science,
  National University of Singapore, Singapore, 2006

- Bachelor of Science in Material Science,
  Shanghai Fudan University, Shanghai, P. R. China, 2002

Major: Electrical Engineering

Presentations and Publications:

Ruiqiong Li and Haim Grebel,
"Surface Enhanced Fluorescence (SEF): The Effect of Local Polarization States," IEEE Sensors Journal, submitted, November 2008.

Ruiqiong Li, A. Marek, Alex I. Smirno and Haim Grebel,
"Fluorescence Detection of Protein Bound to Lipid Bilayers when Incorporated within Nano-Pores," Journal of Chemical Physics, Vol. 129, 095102, 2008.

Amrita Banerjee, Ruiqiong Li and Haim Grebel,
"Raman Spectrum of Graphene Coated Nano-Holes," Material Research Society Symposium Proceedings, Vol. 1059, 1059-KK10-26, 2008.

To my family, for their love, support and encouragement

ACKNOWLEDGMENT

I would like to gratefully acknowledge those who helped to make this project possible. First of all, I would like to express my sincere gratitude to my advisor and mentor, Dr. Haim Grebel, for his continuous guidance and invaluable advice during the course of my research study. The scientific analysis methods and research skills imparted by him are beneficial to me for my future research work.

Special thanks are given to my committee members, Dr. Leonid Tsybeskov and Dr. Raquel Perez-Castillejos, for their constructive discussion, suggestion and careful reviews of this research.

In addition, I would like to thank my lab mates in the Electronic Imaging Center (EIC) and my friends at NJIT. The time we spent together is the source of good memory in my life.

Last but not least, I am deeply indebted to my husband, Dr. Si Yin, for his love, sacrifice, and constant support. My deepest appreciation also goes to my parents, for their thoughtful understanding, unceasing encouragement and endless moral support throughout the years.

TABLE OF CONTENTS

TABLE OF CONTENTS

(Continued)

LIST OF FIGURES

LIST OF FIGURES

LIST OF FIGURES

Figure **Page**

NOMENCLATURE

ABBREVIATIONS

1D	One-Dimensional
2D	Two-Dimensional
3D	Three-Dimensional
AAO	Anodized Aluminum Oxide
AFM	Atomic Force Microscopy
DI	De-Ionized
FESEM	Field Emission SEM
PBE	Photonic Band Edge
PBG	Photonic Band Gap
PMT	Photomultiplier Tube
SEF	Surface Enhanced Fluorescence
SEM	Scanning Electron Microscopy
SP	Surface Plasmons
SPM	Scanning Probe Microscope
SPR	Surface-Plasmon Resonance
SPW	Surface Plasmon Wave

NOTATION

$\vec{E}$	Electric field vector
$\vec{B}$	Magnetic induction vector
$\vec{D}$	Electric displacement vector
$\vec{H}$	Magnetic field vector
ε	Dielectric constant

ε_0	Dielectric constant of vacuum (8.854×10^{-12} F/m^2)
ε_r	Relative dielectric constant
μ	Magnetic permeability
μ_0	Magnetic permeability of vacuum ($4\pi\times10^{-7}$ H/m^2)
μ_r	Relative magnetic permeability
n	Refractive index
ω	Frequency
k	Wave number
β	Propagation constant
ε_m	Permittivity of the metal
ε_d	Permittivity of the dielectric material
δ_d	Decay length into the dielectric medium
δ_m	Decay length into the metal
a	Lattice constant
G	Reciprocal lattice vectors
θ	Tilt angle
ϕ	Azimuthal angle
q	Integer (both negative and positive numbers are allowed)
λ	Wavelength
n_{eff}	Effective index of refraction for the surface plasmon wave
D_{int}	Inter-pore distance
V_a	Anodization voltage
D_p	Packing density
$\Delta\eta$	Phase difference between the grating and the propagating beam

CHAPTER 1

INTRODUCTION

1.1 Background

Anodized aluminum oxide (AAO) (Figure 1.1) has attracted much interest during past few decades for its highly ordered hexagonal structure of nano-holes. Taking advantage of the high extinction ratio of the holes, AAO substrates were typically used as templates for the fabrication of quasi one-dimensional structures for electronic, optoelectronic and micromechanical devices [1-3]. Recently, we have reported on novel spectroscopic applications with AAO substrates: these were used as platforms which enhance weak Raman [4, 5] or, fluorescence signals [6]. Such platforms could be of particular importance for detecting biological species such as DNA, and for signal enhancement of fluorescence based biochip.

Surface plasmons (SP) are near field phenomena: surface charge waves are confined to an interface between metal and dielectric. Periodic structures are often utilized to couple light to these surface waves. In these structures, the lattice constants are typically one-half of either the exciting or the excited (scattered) optical wavelength [7]. Metallic colloids and metal corrugations have been used to enhance Raman and fluorescence signal, as well. Their disadvantage though is that a likely local stress, induced by the nano-size structures may distort the Raman spectra of molecules under test [8, 9]. This is particularly true for soft biospecies, such as, DNA and to a larger extend for protein biomarkers, which are even more fragile. On the other hand, aluminum/aluminum oxide surfaces exhibit advantages over corrugated surfaces. Under ambient conditions the aluminum surface is rapidly oxidized forming nanoscale-thin but

durable aluminum oxide film. This oxide surface is biocompatible [10] and is suitable for stabilizing lipid bilayers with minimal perturbations [11-13]. In addition, aluminum surface could be anodized to produce macroscopically homogeneous and hexagonally packed nanopores with diameter tunable within the ca. 4 - 200 nm range [14-16]. The length of the pores could also be varied from ca. 0.5 to more than 100 μm. In this thesis, we demonstrate the utility of nano-structured aluminum/aluminum oxide platform for biosensing by fluorescence spectroscopes.

Detection and fingerprinting of a wide range of analytes from volatile chemicals to bio-molecules such as, DNA, proteins, and their complexes is a long sought goal. Therefore, improvements in the experimental methods for detecting binding interactions between biological macromolecules, which are under conditions that closely mimic cellular environment, are driven by such needs in many fields. These include fundamental biophysical and biomedical studies and practical applications in drug discovery and biosensing. One versatile approach for studying such highly specific binding events is based on immobilizing biological macromolecules on a surface, exposing the functionalized surface to potential ligands, and detecting ligand binding through either specific labeling or by one of the available label-free methods. The most widespread label-free detection systems found on the market are based on surface-plasmon resonance (SPR) [17]. Biochemical interactions at the sensor surface are monitored by observing the changes in resonant behavior of guided waves at a thin metal/dielectric interface. As explained before, surface plasmon resonance is a charge-density oscillation that may exist at such interface. The charge density wave, associated with an electromagnetic wave

reaches its maxima at the interface and decay evanescently into both media. Therefore, the wave is sensitive to events occurring at or at close proximity to such interface.

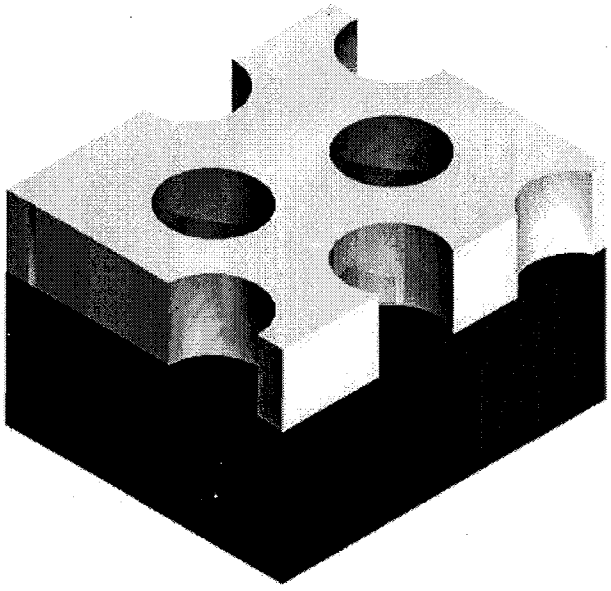

(a)

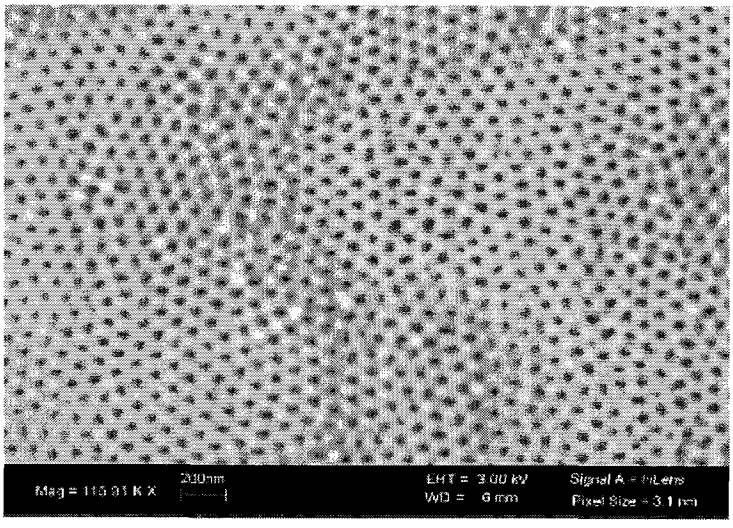

(b)

Figure 1.1 (a) Artistic view of AAO and (b) SEM picture of its realization.

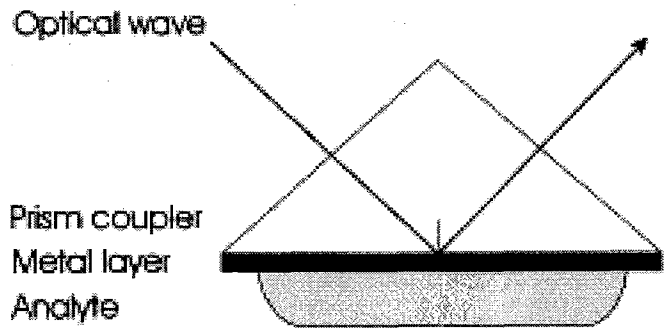

(a)

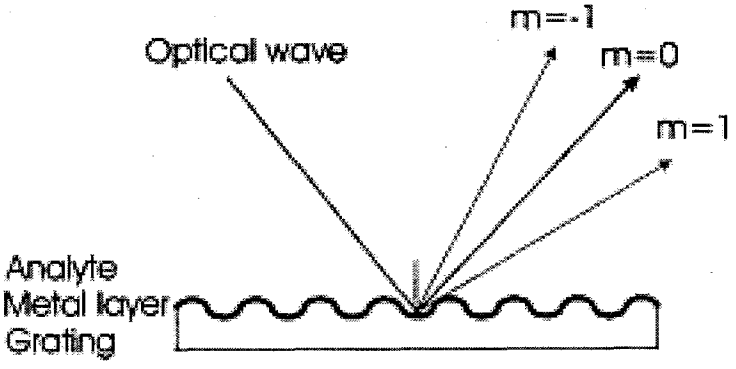

(b)

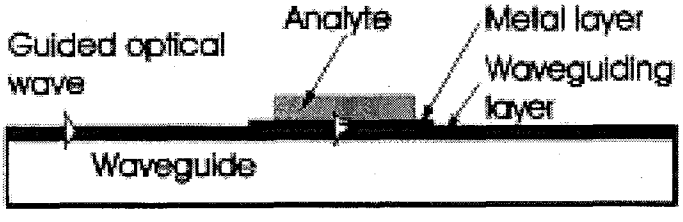

(c)

Figure 1.2 Most widely used configurations of SPR sensors: (a) prism coupler-based SPR system; (b) grating coupler-based SPR system; and (c) optical waveguide-based SPR system.

Figure 1.2 depicts three kinds of the most used SPR sensor configurations. In the prism coupler-based SPR system, a light ray is totally reflected at the interface between a prism coupler and a thin metal layer and excites a surface plasmon wave (SPW) at the outer boundary of the metal by evanescently tunneling through the thin metal layer. For SPR sensors using grating couplers, a metal-dielectric interface is periodically patterned: the incident optical wave is diffracted, forming a series of beams directed away from the surface at a variety of angles. The component of momentum of these diffracted beams along the interface differs from that of the incident wave by multiples of the grating wave vectors. In optical waveguide SPR system, a light wave is guided by the waveguide and, entering the region with a thin metal overlayer; it evanescently penetrates through the metal layer. If the SPW and the guided mode are phase-matched, the light wave excites an SPW at the outer interface of the metal.

While the SPR method is widely applied for biosensing, there is still a need for further development in several directions such as; (1) improvement of detection limits and (2) development of advanced recognition methods. Typically, these directions are pursued separately. For example, improvements of detection sensitivity could be achieved through further optimization of SPR optical instruments and the development of efficient referencing concepts and sophisticated data processing methods [17]. Other researchers have focused on exploring SPR phenomena in nanostructures that deviate significantly from traditionally employed surfaces [18-22]. For example, a quasi three-dimensional structure in the sub-micron scale has been proposed for imaging and monitoring of label-free binding events [23]. In separate efforts researchers have focused on developing recognition elements and matrices that will be suitable for immobilizing

biological macromolecules in functional conformations that ensure analyte binding. A wide range of nanocoatings including planar monolayers and three-dimensional hydrogels that could be applied for metal surfaces of SPR sensors as well as other substrates have been explored [24, 25]. For example, electrostatic immobilization of DNA on a surface positively charged poly-L-lysine layers has been proven to be useful [24].

1.2 Objectives and Outline

As mentioned before, AAO films are composed of highly ordered hexagonal structure of nano-holes. Such periodic structure may be utilized to couple light into propagating surface waves. Under certain conditions, such waves may be utilized to enhance the Raman and fluorescence signals of molecules. The overall objective of this thesis is to develop a biosensing platform for detecting binding events of protein to cell membrane. As a first step we investigate the effect of incident polarization and sample orientation on the fluorescence signals of several test molecules.

The thesis is outlined as follows. Chapter 2 reviews the theoretic background of SPW in patterned substrates. Chapter 3 describes the experimental procedure adopted in this thesis and the characterization method used to analyze the structures: these include scanning electron microscopy (SEM), atomic force microscopy (AFM) and fluorescence spectroscopy. In Chapter 4, the fluorescence of protein, which is bound to nanopore-confined lipid bilayer, is examined under various rotation conditions. The effect of linearly polarized incident beams on the fluorescence of dye imbedded AAO was

examined as well. Chapter 5 discusses the gain and linewidth narrowing in AAO bound plasmonic waveguides. The thesis concludes with a summary in Chapter 6.

CHAPTER 2

THEORETICAL BACKGROUND

This Chapter starts with a brief overview of the basic theory and principles of electromagnetism that are applied in this project. An overview of Maxwell's equations as applied to linear, isotropic and nonmagnetic media and the principal boundary conditions of the field components is given. The wave equation for solving longitudinally invariant waveguides is derived from Maxwell's equations and its solution is discussed, as well in Section 2.1. Surface plasmon subwavelength optics is discussed in Section 2.2. A brief description of photonic crystals is provided in Section 2.3. Further theoretic considerations as pertinent to this work will be presented in Section 2.4.

2.1 Electromagnetic Theory

Optical fields are fully described by Maxwell's equations. In a source of free media Maxwell's equations are as following [26]:

$$\nabla \times \vec{E} = -\frac{\partial \vec{B}}{\partial t} \tag{2.1}$$

$$\nabla \times \vec{H} = \frac{\partial \vec{D}}{\partial t} \tag{2.2}$$

$$\nabla \cdot \vec{D} = 0 \tag{2.3}$$

$$\nabla \cdot \vec{B} = 0 \tag{2.4}$$

The vector quantities are the electric field vector $\vec{E}$ (V/m), the magnetic induction vector $\vec{B}$ (T), the electric displacement vector $\vec{D}$ (C/m^2) and the magnetic field vector $\vec{H}$ (A/m). Eqs. (2.1) and (2.2) are vector equations that relate time and space derivatives of the field

quantities and Eqs. (2.3) and (2.4) are scalar equations that give information about the outflow of the electric and magnetic field.

In linear and isotropic media $\vec{D}$ and $\vec{B}$ are defined as

$$\vec{D} = \varepsilon \vec{E} \tag{2.5}$$

$$\vec{B} = \mu \vec{H} \tag{2.6}$$

with $\varepsilon = \varepsilon_0 \varepsilon_r$ and $\mu = \mu_0 \mu_r$.

The quantities ε and μ define the electromagnetic properties of the medium and are the dielectric constant and magnetic permeability of the medium, respectively. Meanwhile, ε_0 is the dielectric constant of vacuum (8.854×10^{-12} F/m^2), ε_r is the relative dielectric constant of material; μ_0 is the magnetic permeability of vacuum ($4\pi\times10^{-7}$ H/m^2) and μ_r is the magnetic permeability of the material. In the present work, only non-magnetic materials are considered, such that μ_r =1 throughout. When analyzing the optical properties of a material it is convenient to work with its refractive index, n, which is defined as $n = \sqrt{\mu_r \varepsilon_r}$.

Maxwell's equations of the form (2.1-2.4) are valid for regions of continuous physical properties. In the case where the properties of the material changes abruptly, quantities such as $\vec{E}$, $\vec{H}$, $\vec{B}$ and $\vec{D}$ have to satisfy certain boundary conditions. A typical situation is shown in Figure2.1. $\vec{E}_1$ and $\vec{H}_1$ are the electric and magnetic field in the medium 1 characterized by ε_1, μ_1. $\vec{E}_2$ and $\vec{H}_2$ are the corresponding fields in the medium 1 to the medium 2. In the case when surface charges and surface currents are absent, the boundary conditions are reduced to:

a) Tangential components of electric field are continuous,

$$\vec{n} \times \vec{E}_1 = \vec{n} \times \vec{E}_2 \tag{2.7}$$

b) Tangential components of magnetic field are continuous,

$$\vec{n} \times \vec{H}_1 = \vec{n} \times \vec{H}_2 \tag{2.8}$$

c) Normal components of electric flux are continuous,

$$\vec{n} \cdot \vec{D}_1 = \vec{n} \cdot \vec{D}_2 \tag{2.9}$$

d) Normal components of magnetic flux are continuous,

$$\vec{n} \cdot \vec{B}_1 = \vec{n} \cdot \vec{B}_2 \tag{2.10}$$

In non-magnetic media ($\mu_1 = \mu_2 = \mu_o$) Eq. (2.10) is reduced to

$$\vec{n} \cdot \vec{H}_1 = \vec{n} \cdot \vec{H}_2 \tag{2.11}$$

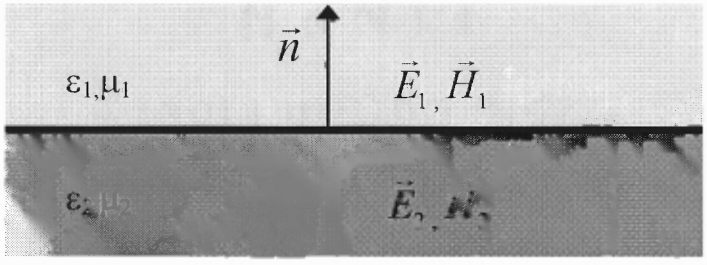

Figure 2.1 Discontinuity in material properties

The total electromagnetic field that is supported by the waveguide can be expressed in terms of only electric or magnetic field components to produce wave equations. The wave equations are derived starting from Maxwell's equations, assuming that the fields vary with time as $e^{j\omega t}$. Taking the curl of Eq. (2.1) and replacing time derivatives with $j\omega$ gives,

$$\nabla \times \nabla \times \vec{E} = k^2 \vec{E} \tag{2.12}$$

where $k^2 = \omega^2 \varepsilon \mu$ is the wave number.

Using the identities

$$\nabla\times\nabla\times=\nabla\nabla\cdot-\nabla^2 \text{ and } \nabla\cdot(\varepsilon\vec{E})=\varepsilon\nabla\cdot\vec{E}+\vec{E}\cdot\nabla\varepsilon=0 \tag{2.13}$$

the wave equation for the electric field is obtained in the form

$$\nabla^2\vec{E}+\nabla\left(\frac{\vec{E}\cdot\nabla k^2}{k^2}\right)+k^2\vec{E}=0 \tag{2.14}$$

Similarly, the wave equation expressed in terms of the magnetic field is

$$\nabla^2\vec{H}+k^2\left(\nabla\cdot\frac{1}{k^2}\right)\times\left(\nabla\times\vec{H}\right)+k^2\vec{H}=0 \tag{2.15}$$

Eqs. (2.14) and (2.15) are vector wave equations in which the dielectric constant is assumed to be a function of all three coordinates, i.e., ε=ε(x, y, z). The vector wave equations are solved subject to the requirements that fields decay away from the guiding region and satisfy appropriate boundary conditions at any discontinuity interface. This leads to an eigenvalue equation which is solved for the propagation constant β.

Further simplification can be introduced by assuming that waveguides are longitudinally invariant i.e., $\frac{\partial\varepsilon}{\partial z}=0$, which is the case in most practical structures. One typical waveguide structure is shown in Figure 2.2 where n_1 is the refractive index of the core and n_2 the refractive index of the cladding which is assumed unbounded. In this case the total field can be expressed in terms of transverse components of electric (E_x and E_y), or magnetic field (H_x and H_y). The rest of the field components can be derived from Maxwell's equations (2.1)-(2.4). For example, if the E-field formulation is used the E_z component is found from Eq. (2.3) and magnetic field components from Eq. (2.1). If using the H-field formulation Eqs. (2.4) and (2.2) will provide the rest of the field components.

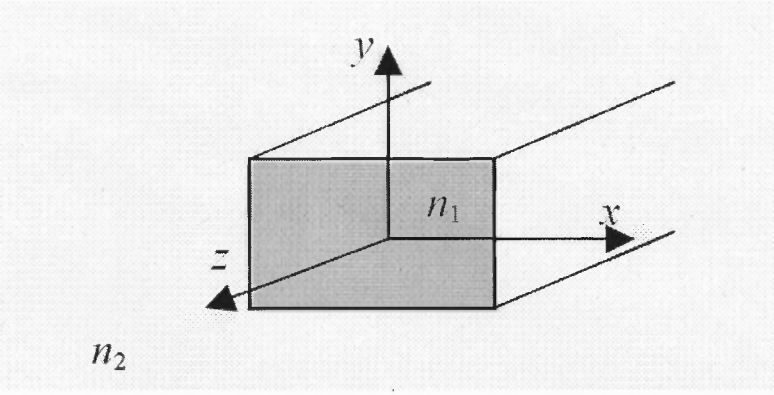

Figure 2.2 Cross section of a waveguide

Hence, from Eq. (2.14), the transverse electric field components satisfy

$$\frac{\partial^2 E_x}{\partial x^2}+\frac{\partial^2 E_x}{\partial y^2}+\frac{\partial^2 E_x}{\partial z^2}+\frac{\partial}{\partial x}\left(\frac{1}{k^2}E_x\frac{\partial k^2}{\partial x}\right)+k^2E_x=-\frac{\partial}{\partial x}\left(\frac{1}{k^2}E_y\frac{\partial k^2}{\partial y}\right) \tag{2.16}$$

$$\frac{\partial^2 E_y}{\partial x^2}+\frac{\partial^2 E_y}{\partial y^2}+\frac{\partial^2 E_y}{\partial z^2}+\frac{\partial}{\partial y}\left(\frac{1}{k^2}E_y\frac{\partial k^2}{\partial y}\right)+k^2E_y=-\frac{\partial}{\partial y}\left(\frac{1}{k^2}E_x\frac{\partial k^2}{\partial x}\right) \tag{2.17}$$

From Eq. (2.15) the transverse magnetic field components satisfy

$$\frac{\partial^2 H_x}{\partial x^2}+\frac{\partial^2 H_x}{\partial y^2}+\frac{\partial^2 H_x}{\partial z^2}+k^2\frac{\partial}{\partial y}\left(\frac{1}{k^2}\right)\frac{\partial H_x}{\partial y}+k^2H_x=-k^2\frac{\partial}{\partial y}\left(\frac{1}{k^2}\right)\frac{\partial H_y}{\partial x} \tag{2.18}$$

$$\frac{\partial^2 H_y}{\partial x^2}+\frac{\partial^2 H_y}{\partial y^2}+\frac{\partial^2 H_y}{\partial z^2}+k^2\frac{\partial}{\partial x}\left(\frac{1}{k^2}\right)\frac{\partial H_y}{\partial x}+k^2H_y=-k^2\frac{\partial}{\partial x}\left(\frac{1}{k^2}\right)\frac{\partial H_x}{\partial y} \tag{2.19}$$

The vector field equations give an accurate representation of the propagating field but in many practical cases they can be simplified by assuming certain approximations to the propagating field. Depending on the level of approximation two different types of field can be distinguished: the semi-vectorial and the scalar fields.

The semi-vectorial field is a five component field solution in which one transverse electric or transverse magnetic field component is assumed to be zero. Two different polarizations can be distinguished: the TE-polarization (s-polarization) and the TM-

polarization (p-polarization) (Figure 2.3). Thus, in the case of semi-vectorial fields the right hand side of Eqs. (2.16)-(2.19) becomes zero, i.e. polarization coupling vanishes. For each polarization, the semi-vectorial wave equations can be cast in either *E*-field or *H*-field forms. In the TE case, the E_y or H_x terms are assumed zero, and the resultant wave equations are:

$$\frac{\partial^2 E_x}{\partial x^2}+\frac{\partial^2 E_x}{\partial y^2}+\frac{\partial^2 E_x}{\partial z^2}+\frac{\partial}{\partial x}\left(\frac{1}{k^2}E_x\frac{\partial k^2}{\partial x}\right)+k^2E_x=0 \tag{2.20}$$

$$\frac{\partial^2 H_y}{\partial x^2}+\frac{\partial^2 H_y}{\partial y^2}+\frac{\partial^2 H_y}{\partial z^2}+k^2\frac{\partial}{\partial x}\left(\frac{1}{k^2}\right)\frac{\partial H_y}{\partial x}+k^2H_y=0 \tag{2.21}$$

In the TM case, the E_x or H_y terms are zero and the wave equations are:

$$\frac{\partial^2 E_y}{\partial x^2}+\frac{\partial^2 E_y}{\partial y^2}+\frac{\partial^2 E_y}{\partial z^2}+\frac{\partial}{\partial y}\left(\frac{1}{k^2}E_y\frac{\partial k^2}{\partial y}\right)+k^2E_y=0 \tag{2.22}$$

$$\frac{\partial^2 H_x}{\partial x^2}+\frac{\partial^2 H_x}{\partial y^2}+\frac{\partial^2 H_x}{\partial z^2}+k^2\frac{\partial}{\partial y}\left(\frac{1}{k^2}\right)\frac{\partial H_x}{\partial y}+k^2H_x=0 \tag{2.23}$$

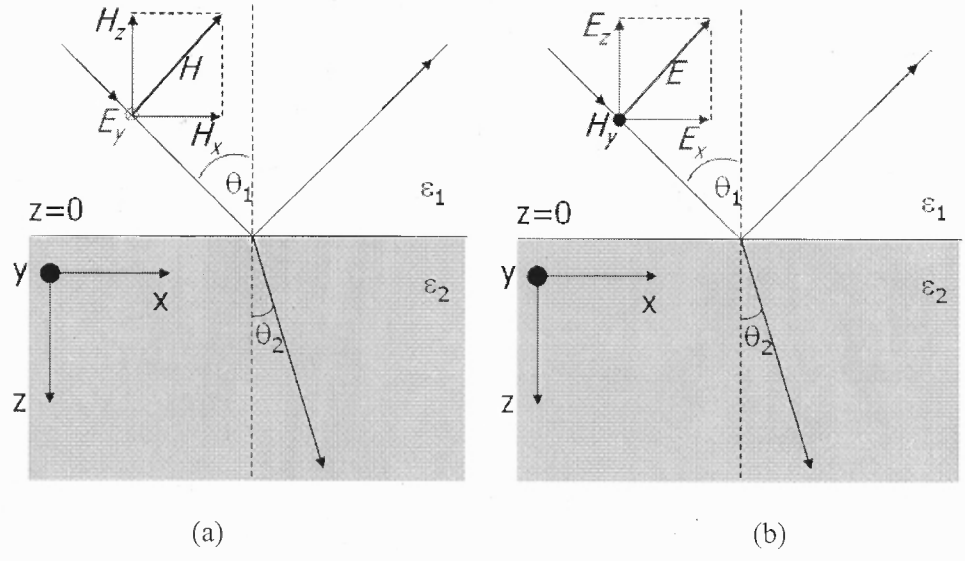

(a) (b)

Figure 2.3 (a) TE polarization (s-polarization): *E*-field is perpendicular to the plane of incidence. (b) TM polarization (p-polarization): *E*-field is parallel to the plane of incidence.

In regions of piecewise constant refractive index, the full vector equations (2.14) and (2.15), along with the ensuing semivectorial equations (2.20)-(2.23), become simple Helmholtz equations with the appropriate boundary conditions enforced at the dielectric interfaces:

$$\nabla^2\vec{E}+k^2\vec{E}=0 \tag{2.24}$$

$$\nabla^2\vec{H}+k^2\vec{H}=0 \tag{2.25}$$

The interface conditions depend upon the polarizations of the fields and whether the E- or H-field solutions are sought. The very simplest such formulation is the scalar case. This ignores the vector nature of the field and characterizes it in terms of the E_z or H_z components which are tangential to all interfaces. The interface conditions are then simply continuity of the field and its derivative, but the scalar approximation is only valid for small refractive index steps.

2.2 Surface Plasmon

Though dated back to the beginning of the twentieth century, the subject of surface plasmons [27, 28] has regained interest because of technological advancement in lithography and the ability to manipulate structures at the nanoscale [29]. Surface plasmons are near-field phenomena. These electromagnetic waves and surface charges are confined to a surface between a metal and a dielectric as shown in Figure 2.4 (a). The interaction between the surface charges and the electromagnetic field attributes to the SP in two aspects: (1) the interaction between the surface charge density and the electromagnetic fields results in the momentum of the SP mode, $\hbar k_{SP}$, being greater than that of a free-space photon of the same frequency, $\hbar k_0$. Applying Maxwell's equations

(2.1)-(2.4) under the appropriate boundary conditions yields the SP dispersion relation [30]:

$$k_{SP} = k_0 \sqrt{\frac{\varepsilon_d \varepsilon_m}{\varepsilon_d + \varepsilon_m}} \tag{2.35}$$

where ε_m and ε_d are permittivity of the metal and the dielectric material, respectively. (2) In contrast to the propagating nature of SP along the surface, the field perpendicular to the surface decays exponentially with distance from the surface (Figure 2.4(b)). The dispersion relation for surface plasmons relative to a light line is depicted in Figure 2.4 (c). It is necessary for $|\varepsilon_m| > \varepsilon_d$ and $\varepsilon_m<0$ for surface plasmons to be created.

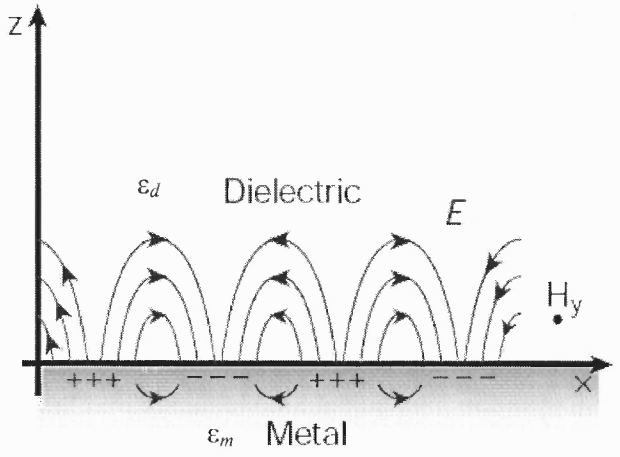

Figure 2.4 (a) SPs are transverse magnetic in character (*H* is in the *y* direction); the generation of surface charge requires an electric field normal to the surface. This combined character also leads to the field component perpendicular to the surface being concentrated near the surface and decaying exponentially with distance away from it

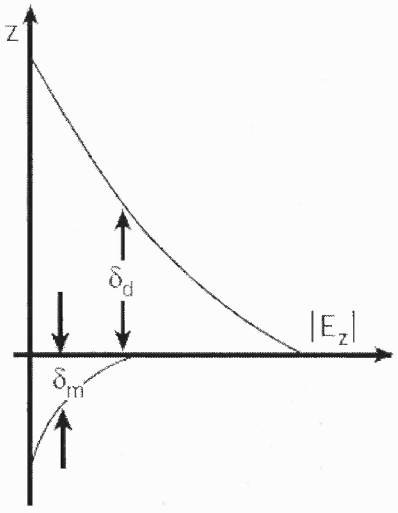

Figure 2.4 (b) The field in this perpendicular direction is said to be evanescent, reflecting the bound, non-radiative nature of SPs, and prevents power from propagating away from the surface. In the dielectric medium above the metal, typically air or glass, the decay length of the field, δ_d, is of the order of half the wavelength of light involved, whereas the decay length into the metal, δ_m, is determined by the skin depth.

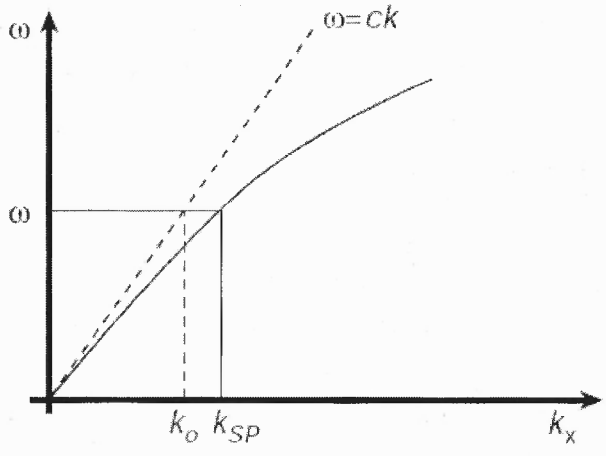

Figure 2.4 (c) The dispersion curve for a SP mode shows the momentum mismatch problem that must be overcome in order to couple light and SP modes together, with the SP mode always lying beyond the light line, that is, it has greater momentum ($\hbar k_{SP}$) than a free space photon ($\hbar k_o$) of the same frequency ω.

Periodic arrays of subwavelength holes are often used to couple the incident light to surface plasmons. For such hole arrays, incident light is scattered by the array, producing evanescent waves that tunnel through the holes, resulting in a small but finite amplitude on the far side of the array (the metal). The evanescent waves are reflected and the interference of the resulting waves produces a wave that is partially propagating away from the structure and partially propagating along the surface (hence the SP waves). The electric field intensity is concentrated in the holes at the oxide/air interface, away from the metal.

2.3 Photonic Crystals

Photonic crystals were recently proposed as a method to control light propagation [31]. These 'crystals' are regular, repeating arrays of contrasting dielectric materials. Figure 2.5 shows schematic views of a variety of photonic crystals with dimensions ranging from 1 to 3. The one-dimensional crystal must have radiation propagating through it in a direction normal to the contrasting dielectric planes for any of the photonic crystal effects to appear. Thus transverse Bragg waveguides do not fall within the definition of a photonic crystal device, at least not for impinging plane waves. On the other hand, devices utilizing multilayered dielectric films are familiar, such as the quarter-wave stack (Bragg reflector) commonly utilized for frequency-selective, high-quality reflection. Once the transition is made from transverse one-dimensional crystal architecture to a two-dimensional architecture, the photonic crystal effect becomes the major contributor to the propagation qualities of the crystal. The exact nature of these qualities is not fully known. Several properties have been predicted or identified by researchers: these include the existence of a photonic bandgap, photon localization and superprism or ultrarefractive effects.

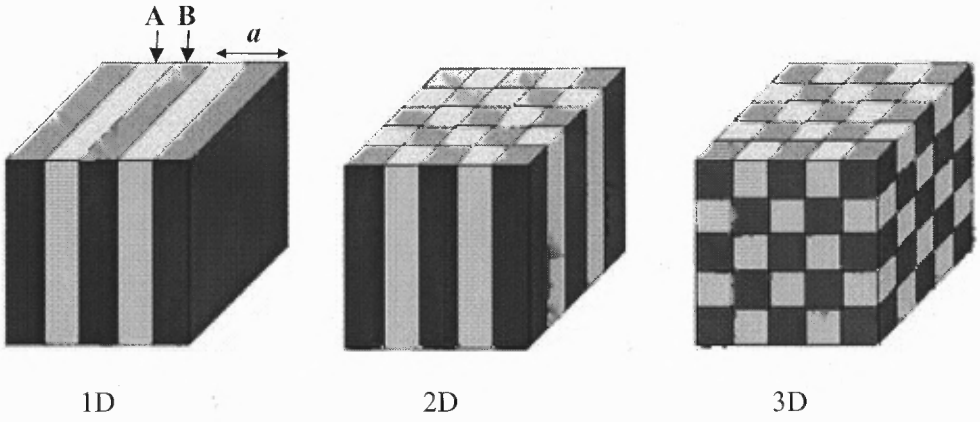

Figure 2.5 Schematic illustration of one-dimensional (1D), two-dimensional (2D), and three-dimensional (3D) photonic crystal. *a* is the lattice constant.

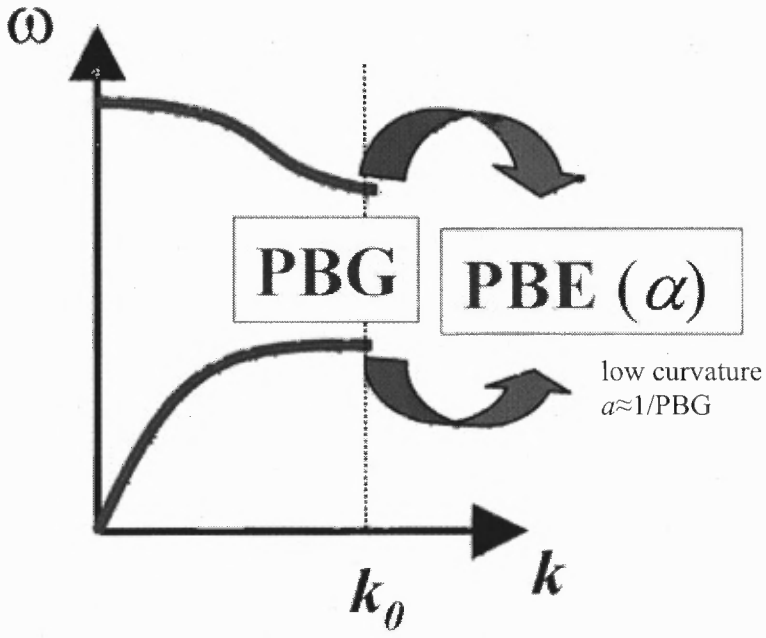

Figure 2.6 Schematic representation of a photonic band gap (PBG) and of related photonic band edge (PBE) in the dispersion characteristics of a photonic crystal.

In the photonic band gap (PBG) scheme (Figure 2.6), the propagation of photons is forbidden for certain frequency range. Moreover, if a disorder is introduced into the regular dielectric structure of the photonic crystal, midgap modes whose eigenfunctions are strongly localized around the disorder may be obtained. These modes are called localized defect modes.

In the photonic band edge (PBE) scheme, the photonic crystal operates around an extreme of the dispersion characteristics where the group velocity of photons vanishes. It should be noted that such dispersion characteristics apply strictly for infinite periodic structure and time. The real world is actually finite and transitory. It is therefore more appropriate to speak in terms of slowing down of optical modes, which remain delocalized.

2.4 Further Theoretic Considerations

The AAO slab may be viewed as a particular case of 2D photonic crystal surface waveguide with hexagonal array of air-rods [32]. There are several limitations to this analogy. (1) The pore packing in AAO is not ideal, especially for commercial AAO, whose pore diameter largely varies; (2) the array pitch is much smaller than the propagating wavelength; and (3) the AAO/Aluminum substrates may be very thick (on the order of 60 μm) with respect to the propagating wavelength (which is true for most commercial AAO substrates). Nevertheless, one could gain some insight by examining an ideal 2D array of holes.

Let us consider an ideal 2D hexagonal case (Figure 2.7) and start by identifying two lattice vectors, $a_1 = \hat{x}a$ and $a_2 = \hat{x}a/2 + \hat{y}\sqrt{3}/2$, where a is the distance between the

nearest neighbor holes. The reciprocal lattice vectors are: $G_1 = \hat{x}2\pi / a - \hat{y}2\pi / a\sqrt{3}$ and $G_2 = \hat{y}4\pi / a\sqrt{3}$. Light is coupled to the periodic array of holes by momentum conservation. For example, if the wave has a propagation component along the *y*-direction, then:

$$k_y + q_2 G_2 = \beta_y \tag{2.36}$$

where, $k_y = k_0 sin(\theta) cos(\phi)$ to account for the tilt θ and the azimuthal ϕ angles; q_2 is an integer (both negative and positive numbers are allowed). Thus, in principle, light may be coupled to surface plasmons in the surface waveguide at a proper tilt angle θ. The coupling efficiency also depends on the in-plane orientation of the hole array with respect to the polarization state of the incident beam.

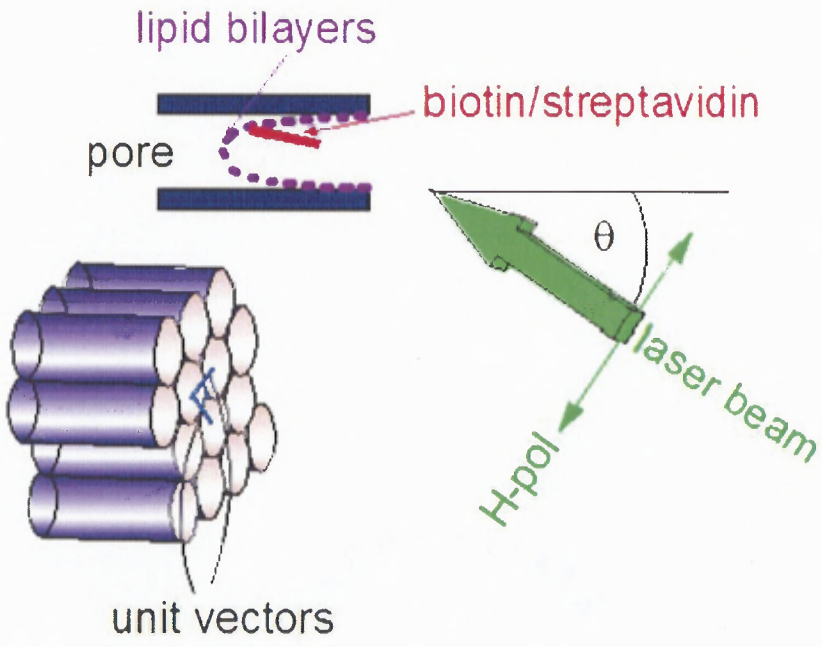

Figure 2.7 Unit vectors and ideal arrangement of holes.

Suppose that the surface component of the wave inside the AAO sample $\boldsymbol{\beta}=\boldsymbol{\beta}(x,y)$ (bold letters are used for vector notations) is scattered from the same periodic structure. This may happen because the AAO is made of densely packed holes with inter hole-spacing which is much smaller than the propagating wavelength. This is also happening because of the abrupt nature of the hole in the AAO slab, invoking higher-orders and sub-orders of diffraction. Some directions within the crystal of holes will strongly diffract the beam when the following phase match condition is fulfilled:

$$|\boldsymbol{\beta}-q\boldsymbol{G}|=\beta \tag{2.37}$$

Again, q is an integer. One can envision that such Bragg diffraction creates a standing wave within the hole-array. These considerations are true for the pump as well as, for the fluorescing wavelengths.

Optimal fluorescence conditions occur when the mode propagating in the AAO is a surface mode. We note that in general the oxide layer is very thin on top of the aluminum. Therefore, from Eq. (2.35), the surface mode propagates at $\beta=k_0[\varepsilon_m\varepsilon_d/(\varepsilon_m+\varepsilon_d)]^{1/2}$ with ε_m the dielectric constant of metal and ε_d the dielectric constant of air. When considering aluminum, the real part of the permittivity has a large negative value, thus, $\varepsilon_m <<0$ and therefore, $\beta\sim k_0$. We also note that the fill factor for the holes is small, approximately 6% and does not affect the propagation constant much. It is obvious that when $\theta=0$ (normal incidence), the propagation constant for a specific wavelength inside the AAO layer has a degeneracy of two counter propagating beams, each fulfilling the condition, $\beta=qG$. This is true for our 2D hexagonal hole-array, with $q_i\boldsymbol{G}_i$ and q_i integer (with both negative and positive values. Therefore, if light is coupled with $q=1$ mode, it may be confined with $q=2$ mode. The idea may be extended to sub-harmonics,

such that, q_i=±1/2, ±1/3....as well [32]), the optimized wavelength, which fulfills this requirement, may be approximated at normal incidence as,

$$\lambda_{opt} = \frac{a}{\sqrt{\left(\frac{4}{3}\right)\cdot\left(q_1^2 - q_1 q_2 + q_2^2\right)}} \cdot \sqrt{\frac{\varepsilon_d \varepsilon_m}{\varepsilon_d + \varepsilon_m}} \tag{2.38}$$

All together, at normal incidence there would be two-fold degeneracy: two beams oscillating in-parallel to the AAO surface. Since we are dealing with sub-harmonics, Eq. (2.38) predicts transverse resonance effect at λ~558 nm for a~90 nm, q_1=1/7, q_2=0. This is very close to the fluorescence peak of fluorescein dye imbedded at the structure pores at λ~560 nm. We note that there are several resonances for this wavelength owing to the close pack symmetry of the hole-array. Eq. (2.38) may be extended for oblique incidence as well:

$$\sin(\theta) = \frac{\lambda_0}{a}\sqrt{\left(\frac{4}{3}\right)\left(q_1^2 - q_1 q_2 + q_2^2\right)} - n_{eff} \tag{2.39}$$

Here, $n_{eff} = \sqrt{\varepsilon_1 \varepsilon_2 / (\varepsilon_1 + \varepsilon_2)}$, the effective index of refraction for the surface plasmon wave. Eq. (2.39) implies that upon a proper tilt, enhancement of the fluorescence may be achieved. In particular, the λ~560 nm line is at resonance with q_1=1/6, q_2=0 planes when the sample is tilted by θ~10°. Moreover, the 514.5 nm line may be effectively coupled to surface plasmons at θ~8°. This raises the possibility that the both of the pump and the fluorescence wavelengths be launched and detected simultaneously.

Let us consider a surface mode, which propagates parallel to the slab surface. If the photonic crystal is made perfect, then, there exists a bandgap for some frequencies. Namely, the propagation of these frequencies would be frustrated for all crystallographic

directions (or, throughout the Brillouin zone and its sub-harmonics). If the arrangement of holes is far from ideal and we operate at frequencies outside the bandgap, the reflections from the hole-array in some directions within the *x-y* plane will be stronger than the others and will depend on the crystallographic symmetry of the holes. Thus, for normally incident beam, fluorescing signals which are generated by molecules imbedded in the structure will depend on the in-plane rotation angle with respect to the linearly polarized incident wave [33]. The symmetry of the hole-array will dictate the number of cycles upon full azimuthally sample rotations. For hexagonal array of holes there would be symmetry of 60^{o} or its multiple. On the other hand, at transverse resonance conditions, there ought to be period doubling [33] which is the result of multiple reflection by the transverse resonating effect.

To summarize, the efficiency of the coupling between the hole array and the polarization state of the incident pump beam depends on the coherence of the scattering process. A proper tilt angle ensures coupling to a surface mode and in-plane rotations provide for the proper phase match conditions.

CHAPTER 3

EXPERIMENT AND METHODS

In this chapter, the experimental procedure for AAO film fabrication is described in Section 3.1. The properties of commercial AAO are examined in Section 3.2. The preparation of protein bound to lipid bilayers, which are incorporated within nano-holes is presented in Section 3.3. In addition, the characterization methods with respect to the optical and structural properties of AAO are presented. The characterization techniques include scanning electron microscopy (SEM), atomic force microscopy (AFM) and surface enhanced fluorescence (SEF). They are briefly discussed in Section 3.4.

3.1 Fabrication of AAO Film

In this work, ordered nano-holes anodic oxide films on aluminum were fabricated according to a well-established recipe [34, 35]. The formation mechanism of AAO, the factors for AAO formation and the process of AAO fabrication are briefly discussed in the following three subsections.

3.1.1 Formation Mechanism of AAO

Since the first observation of the porous nature of alumina films produced in certain electrolytes, several theories have been proposed to account for the pore formation. After 30 years investigation, the evidence that the electrolyte plays an important part in the formation of porous films has established by Sullivan *et al* [36]. As illustrated in Figure 3.1, during steady state conditions, pores grow perpendicular to the surface with

equilibrium of field-enhanced oxide dissolution at oxide/electrolyte interface and oxide growth at the metal/oxide interface. While the latter is due to the migration of oxygen containing ions (O^{2-}/OH^-) from the electrolyte through the oxide layer at the bottom, Al^{3+} ions, which simultaneously drift through the oxide layer, are ejected into the solution at oxide/electrolyte interface [37]. The fact that Al^{3+} ions are lost to the electrolyte has been shown to be a prerequisite for porous oxide growth, whereas Al^{3+} ions, which reach the oxide/electrolyte interface, contribute to oxide formation in the case of barrier oxide growth [38, 39].

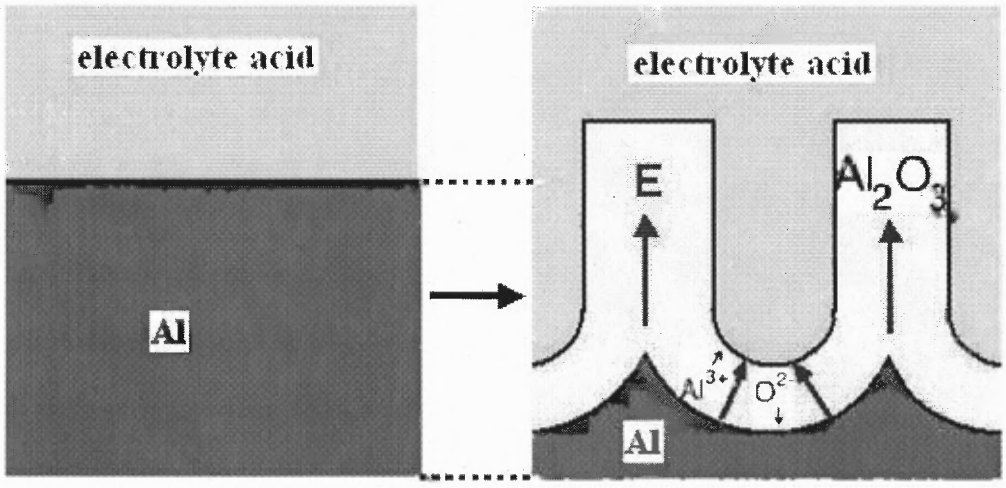

Figure 3.1 Illustration of the formation mechanism of AAO.

The overall reaction that takes place during anodization is:

$$2Al+3H_2O \rightarrow Al_2O_3+3H_2$$

The reactions at the anode occur at the metal/oxide and oxide electrolyte interfaces. At the metal/oxide interface the inward moving oxygen anions react with metal:

$$2Al+3O^{2-} \rightarrow Al_2O_3+6e^-$$

At the oxide/electrolyte interface outward moving aluminum cations react with water:

$$2Al^{3+}+3H_2O \rightarrow Al_2O_3+6H^+$$

The reaction at the cathode is hydrogen gas generation:

$$6H^++6e^- \rightarrow 3H_2$$

The atomic density of aluminum in alumina is lower by a factor of two than in metallic aluminum. A possible origin of forces between neighboring pores is therefore mechanical stress associated with the expansion during oxide formation at metal/oxide interface. Since the oxidation takes place at the entire pore bottom simultaneously, the material can only expand the vertical direction, so that the existing pore walls are pushed upwards [38, 39].

3.1.2 Facts for AAO Formation

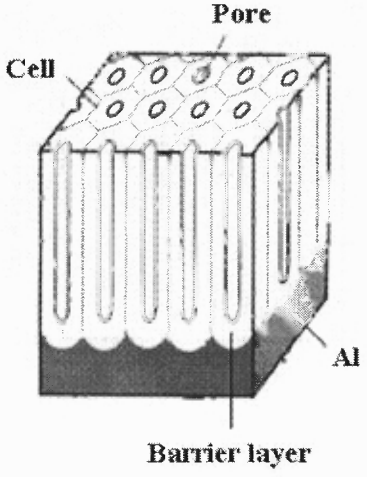

Figure 3.2 Idealized structure of AAO

An idealized sketch of the AAO film structure is shown in Figure 3.2. The oxide has a cellular structure with a central pore in each cell. The sketch shows uniform hexagonal cells, but most anodization conditions produce films with disordered structures, which have a broad distribution of cell size and pore diameter. Anodization under appropriate conditions can produce AAO with a highly ordered cell configuration. This process is characterized by proper concentration of the electrolytes and anodizing voltage, longer anodization period, a smooth surface of Al, and low anodization temperature.

Electrolytes and Anodization Voltage

Of all the fabrication parameters, electrolyte types and concentration, as well as anodization voltage have the strongest impact on the AAO structure. Self-organization has been found in three types aqueous electrolytes: sulfuric, phosphoric and oxalic acids. There is certain optimum anodization voltage and solution concentration for each type of electrolyte. For example, the most appropriate anodization condition for oxalic acid solution is in a concentration of 0.3 M with a constant voltage of 40 V [35].

In this thesis, oxalic acids have been chosen as electrolytes for AAO fabrication. The selection of the applied voltage is based on fact that the AAO cell size has a good linear relationship with the applied voltage, where the proportionality constant of the inter-pore distances per applied voltage is approximately 2.5 nm/V [40, 41]. The empirical formula is written as following:

$$D_{int}=2.5V_a \tag{2.1}$$

where D_{int} is the inter-pore distance (cell size) in nm, and V_a is the anodization voltage in V. The packing density of the pores can be derived from the inter-pore distance as following:

$$D_p = \frac{2}{\sqrt{3}D_{int}^{\ 2}} \tag{2.2}$$

where D_p is the packing density.

Anodization Time

It was found that a long period of anodization time can improve the regularity of the cell arrangement. Defect-free regions appear in large domains, whereas defects are found at the boundaries of these domains. That is, the size of the defect-free region increases with the anodization time. Even at the deficiency site of the concave, pores can be compensated automatically and almost perfect arrangement of the pore configuration can be recovered after a long anodization period. This is because the pores at deficient sites tend to develop and recover the closest packing arrangement of the cylindrical cells, which is the most probable arrangement in the cell configuration of the AAO.

Surface Roughness

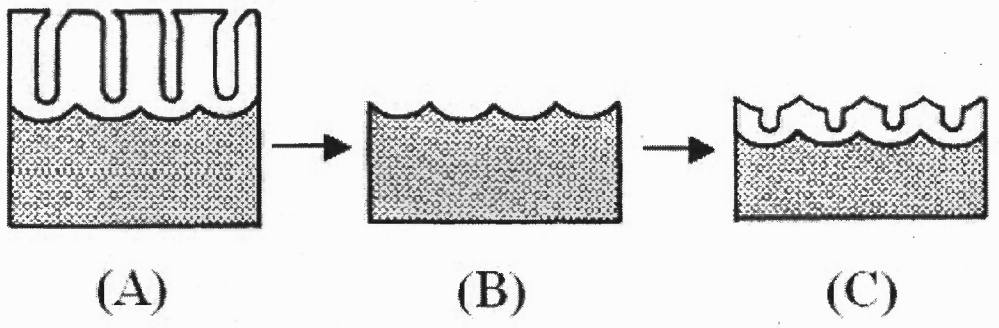

Figure 3.3 Schematic diagrams for two-step fabrication of AAO membrane. (A) AAO after first anodization. (B) Removal of AAO layer. (C) Initiation of hole formation in second anodization.

Surface roughness of the initial Al had not been considered important. As demonstrated previously, even with a rough initial surface, almost ideally arranged hexagonal structure

can be obtained after long anodization time. However, in order to get perfect AAO pore arrangement, two-step anodizing fabrication was proposed to improve the surface roughness [35]. Schematic diagrams for such processes are shown in Figure 3.3. For the first step, the samples are anodized for a long time to obtain a perfect ordered structure at the bottom. Then, the oxide layer is removed by a mixture of phosphoric acid and chromic acid. After removal of the anodic oxide layer, a textured pattern of concaves is obtained on the surface of the Al substrate. This textured Al sample is anodized again at the same cell potential as used during the first anodizing step. Each concave of the surface results in ordered formation of the nano-holes. Though the details of such mechanism is not clear at present, it is generally believed that each convex can induce the independent formation of a hole due to its geometrical effect.

Anodization Temperature

Apart from the electrolytes, anodization voltage, anodization time and surface roughness, the anodization temperature is also an influential factor. Due to the fact that heat generation during anodization process will disturb the stable oxide growth and destroy the formed oxide film, it is very crucial to maintain the anodization process at low temperature.

3.1.3 Process of AAO Fabrication

Figure 3.4 illustrated the setup of AAO fabrication. High purity Aluminum (99.999+%, 0.25 mm thickness) from Sigma-Aldrich was ultrasonically cleaned in de-ionized (DI) water for 30 minutes, and then it was degreased in acetone for more than 24 hours. After a rinse in ethanol, the samples were electropolished in a mixture of ethanol, $HClO_4$ and

DI water at 5 °C and 50 V to decrease surface roughness. Anodization was carried out at 35 V and 5 °C in a 0.3 M oxalic acid for 6–8 hours. Aluminum and Pt were serving as anode and cathode separately. Then, the anodic oxide layer was removed in a mixture of phosphoric acid (6 wt %) and chromic acid (1.8 wt %) at 65 °C for 3 hours. The Al specimen was later anodized again for 5 min under the same conditions as before.

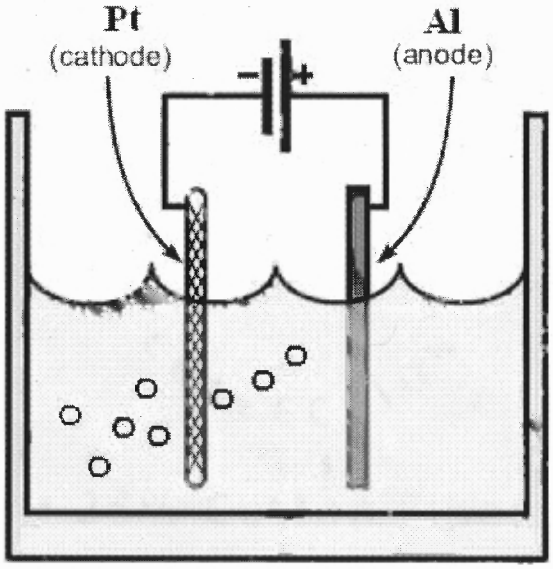

Figure 3. 4 Illustration of AAO fabrication setup.

3.2 Commercial AAO

Some of the experiments were conducted with commercial "0.02 μm" Anodisc 13 membranes (Whatman International, Maidstone, UK) that are shaped as disks of 13 mm in diameter and are about 60 μm thick. Examination of these substrates with SEM (Figure 3.5) yielded an average pore diameter of 177±20 nm on one side, whereas the average diameter for the filtration side was 29±7 nm. Each Anodisc substrate was cut into two halves, one half was flipped, and then the two halves were subjected to the same Au

sputter coating from just the exposed side. The coating was sufficiently thin and did not block the pores. The other side of each half remained uncoated. Such a procedure yielded two types of AAO substrates containing a thin Au layer at either large pore or small pore (filtration) side. Hence, altogether four different nanoporous substrate samples were prepared for depositing lipid bilayers and further analysis. These less ordered AAO substrates were compared to in-house AAO platform (50 nm thick alumina on an aluminum film), which was described in previous subsection. The latter exhibited remarkably periodic array of nanowells [5].

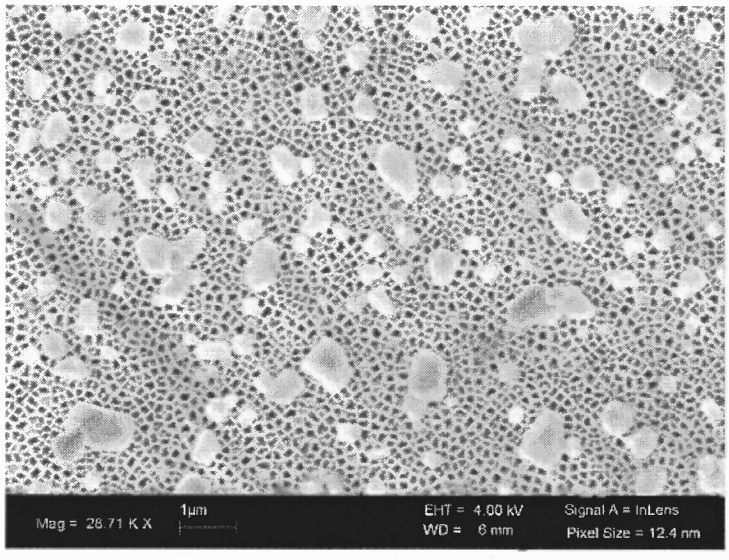

Figure 3.5 SEM image of commercial AAO after depositing streptavidin bound to biotinilated lipid bilayers. The pores are extending throughout the sample (approximately 60 µm thick)

3.3 Lipid Bilayer within AAO

In this work, biotin, bond with streptavidin on lipid bilayers was deposited on AAO (as a platform) and the fluorescence signals from these marked, bio-materials were investigated.

Synthetic zwitterionic phospholipid 1,2-dimyristoylsn-glycero-3-phosphocholine (DMPC) and biotinylated 16:0 Biotinyl Cap PE (1,2-dipalmitoyl-sn-glycero-3-phosphoethanolamine-N-(cap biotinyl), sodium salt) were purchased from Avanti Polar Lipids (Alabaster, Alabama) in chloroform solutions and were stored in a freezer at −80 °C prior to use. Multilamellar vesicles were prepared by mixing chloroform solutions of DMPC and Biotinyl Cap PE in 20:1 or in 200:1 molar ratio. Consequently, chloroform was removed by a rotary evaporator yielding a thin lipid film on the surface of a round bottom flask. Residual chloroform was removed overnight by keeping the flask open to a liquid nitrogen trap and a vacuum pump. Multilamellar vesicles were formed by adding 50 mM Hepes, *p*H 7.0, buffer and cycling the flask for at least ten times between liquid nitrogen at −197 °C (77 K) and a water bath at 30 °C. The final concentration of lipids in aqueous media was 150 mg ml^{-1}.

Streptavidin is a 53 kD tetrameric protein known for its extraordinarily strong affinity for the biotin moiety: the dissociation constant, $K_d \sim 10^{-15}$ mol/L, ranks the biotinstreptavidin complex as one of the strongest among the noncovalent interaction [42]. DTAF-conjugated streptavidin was purchased from Jackson ImmunoResearch Laboratories, Inc. (West Grove, PA) and dissolved in a 50 mM Na/K phosphate buffer at *p*H=7 (VWR International, West Chester, PA). DTAF-conjugated streptavidin was mixed with an excess of biotinylated lipids immediately before the experiments. Each of the

four AAO surfaces described above (namely, two surfaces coated with Au and two uncoated) was exposed to aqueous lipid dispersion while the entire sample was kept at approximately 30 °C to ensure that the lipid membrane is in a fluid bilayer phase. Such an exposure resulted in an immediate wetting of the nanoporous substrate, which became semitransparent. Consequently the samples were allowed to air dry before optical measurements. Previously, we have estimated that such lipid bilayer deposition results in a formation of up to four nanotubular bilayers nestled per each of the nanopore throughout the entire available surface area of the substrate assuming 100% surface coverage [12]. While some of the lipids left on the outside AAO surface were washed away during the preparation, some residual lipids were observed by SEM for the air-dried samples (Figure 3.5). It should be noted here that the condition of full hydration that is essential for lipids to remain assembled into a bilayered structure is likely to break down for the air-dried samples. Therefore, the lipids in such samples are expected to be somewhat disordered and not necessarily assembled into bilayers.

3.4 Characterization Method

Scanning electron microscopy (SEM), atomic force microscopy (AFM) and surface enhanced fluorescence (SEF) were used to characterize the AAO films. These characterization methods are briefly discussed in this section.

3.4.1 Scanning Electron Microscopy (SEM)

The surface morphology of AAO films was observed by the scanning electron microscopy (SEM). The SEM analysis in this work was performed using a LEO 1530VP

field emission SEM (FESEM) with Oxford EDS operating at a maximum voltage of 30 kV. An FESEM incorporates a cold cathode field emission gun, ultra high vacuum, and sophisticated digital technologies for imaging of micro structures. Featuring a conical FE gun and a semi-in-lens objective lens, the system is capable of high resolution imaging as well as high quality real time image display at all scan speeds, enabling observation and recording of superior images even in a bright room.

3.4.2 Atomic Force Microscopy (AFM)

Atomic force microscopy (AFM) is a surface analytical technique which is used to image and explore nanoscale features and structures of surfaces. Digital instrument nanoscope III multimode scanning probe microscope (SPM/AFM) was used in our work. Topography of surfaces can be obtained normally by two different modes, contact mode and tapping mode. In contact mode (Figure3.6), the tip is in perpetual contact with the sample. The tip is attached to the end of a cantilever with a low spring constant, lower than the effective spring constant holding the atoms of most solid samples together. As the scanner gently traces the tip across the sample (or the sample under the tip) union the contact force causes the cantilever to bend and the Z-feedback loop works to maintain a constant cantilever deflection.

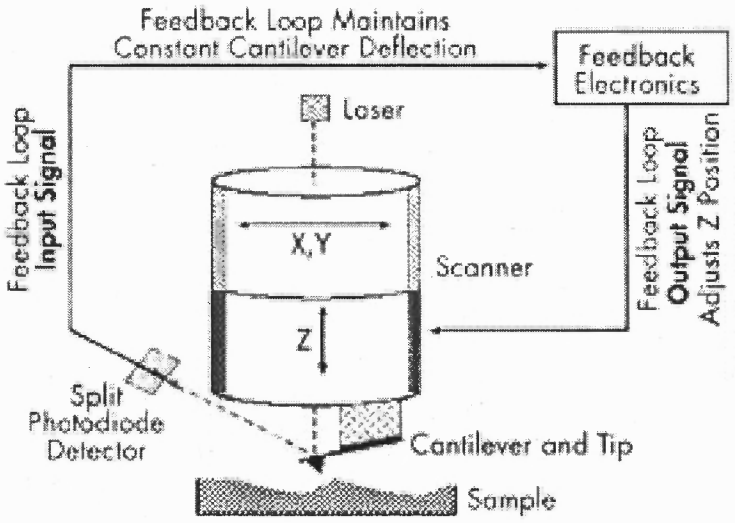

Figure 3.6 AFM tapping mode

3.4.3 Surface enhanced fluorescence (SEF)

In our work, we also investigate the surface enhanced fluorescence on AAO platforms. Fluorescence occurs when a molecule absorbs light from the UV-visible light spectrum, known as excitation, and then, rapidly emits light photons as it returns to its ground state. Fluorescence is the property of electrons in the molecule to absorb light at a special wavelength and emit light at longer wavelengths during an interval called the fluorescence lifetime ($10^{-9} \sim 10^{-7}$ seconds approximately). Fluorescence is widely used to monitor the biochemical reactions though conjugated fluorescing bio-markers.

In the fluorescence experiments, the molecules were deposited on the nano-hole array sample. The sample was mounted on a rotational stage and excited by a 10 mW, 488 nm line or 514.5 nm line of an Ar ion laser. The incident beam was focused to a spot of 50 μm^2 by a 10 cm lens in a confocal configuration (Figure 3.7). An optical low-pass filter in front of the spectrometer (at λ=495 nm or λ=520 nm) ensured the cut off of the

laser line. The scattered light (fluorescence signal) was collimated and focused onto the spectrometer slit. A photomultiplier tube (PMT) was used for detection.

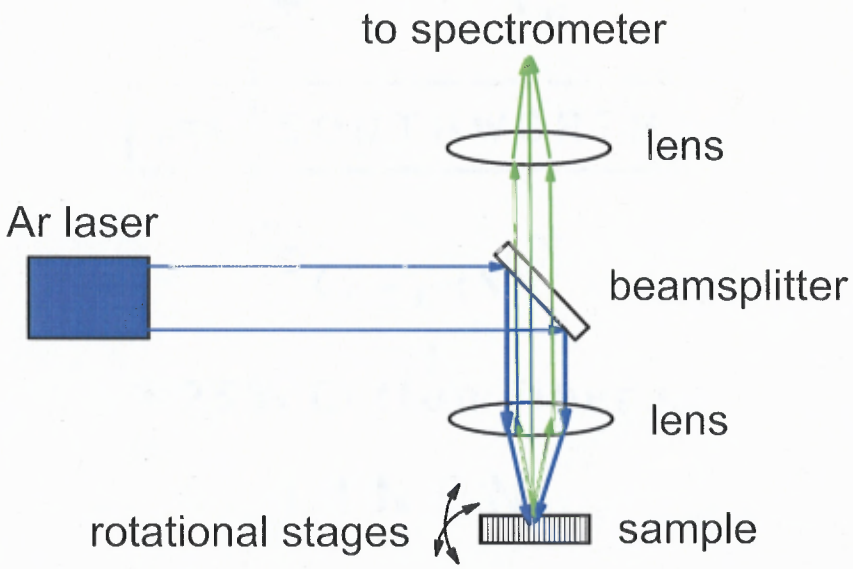

Figure 3.7 System configuration: the pump light (Ar at 488 nm or 514.5nm) is focused onto the sample which is placed on a rotational stage. The fluorescence signal is collimated and focused onto the spectrometer slit. A PMT is used to detect the signal and a cut-off filter is used to eliminate the laser line from the spectra.

CHAPTER 4

FLUORESCENCE ENHANCING PROPERTIES OF NANO-STRUCTURED PLATFORMS

As mentioned before, periodical nano-structure of AAO can be used as spectroscopic signal-enhancing platform. In this chapter, we will explore the possibility of a biosensing platform to enhance the fluorescence signal of proteins bound to lipid bilayers.

Plasma membranes are essential structural elements of eukaryotic cells that define their outer surface. These membranes that are composed from lipids, proteins, and other molecules form highly selective barriers allowing cells to actively control individual biochemical environment at desirable levels. Such environment is cell specific and crucial to the cell function. The active control of intracellular concentrations is achieved by membrane proteins and, primarily, ion channels that respond to various stimuli. Yet, despite growing literature on protein microarrays (see [44] for a review), there are only a relatively few reports on membrane protein arrays and their use for ligand screening [45-47]. Lack of microarray methods for membrane proteins, which represent the single most important class of drug targets, is considered by some as a fundamental limitation to further development of the biochip technology. Previously, it has been shown that lipid bilayers and membrane proteins can be assembled in functional conformations inside macroscopically aligned nanochannels of AAO membranes[11, 13, 48-51]. Cloutier *et al* [52] pointed to the fluorescence enhancing properties of such platforms albeit for optical beams at normal incidence. Firstly, we report on polarization-dependent fluorescence of a protein marker bound to biotinilated lipid bilayers that were deposited into nanochannels of commercial AAO membranes from aqueous dispersions in Section 4.1. While

commercial AAO substrates are easily available, they are known to lack highly ordered honeycomb pore packing and a narrow distribution of pore diameters as achieved with some of our in-house substrates and prepared by a double-anodization method as described in Sec. 3.1.3. Nevertheless, we have found that even these relatively poorly organized commercial AAO membranes are suitable for fluorescence detection of protein binding to lipid bilayers and exhibit unexpected polarization effects. A detail process of the fabrication of lipid bilayer within AAO was discussed in previous Section 3.3. And the system configuration of the fluorescent measurement was presented in Sec 3.4.3.

Our initial hypothesis was that chromophores imbedded in the pores of commercially made nanoporous substrates would not exhibit variations in their fluorescence signals as a function of sample orientation, owing to significant dispersion in the pores' diameter, their shape, the pore packing, and the fact that these pores are much smaller than the interrogating optical wavelengths used. For the experiments we employed zwitterionic lipid bilayers that could be incorporated into nanoporous aluminum oxide membranes with minimal perturbation to the bilayer properties [11, 13, 48-51]. The bilayers were doped with 0.5–5.0 mol % of biotinylated lipids and exposed to 5-(4,6-dichlorotriazinyl)aminofluorescein (DTAF)—a conjugated streptavidin—to mimic protein docking to the membrane surface. Fluorescence signals were measured as a function of the angle between the optical polarization state of the incident beams and the orientations of macroscopically ordered AAO nanochannels.

Our hypothesis was proven wrong: the fluorescence signals varied when pumped with *E*-polarized (*E*-pol or *s*-polarized) and *H*-polarized (*H*-pol or *p*-polarized) incident optical beams. The origin of the observed polarization-dependent effects and the

implications for enhanced fluorescence detection in a biochip format are being discussed in Section 4.1.

In Section 4.2, we extend our study to include in-plane rotations and examine the effect of the crystallography of the hole-array (air-rods) on the fluorescence signal of dye imbedded AAO.

4.1 Polarization-dependent Fluorescence of Protein Bound to Lipid Bilayers within the Pores of AAO

4.1.1 Theoretical Considerations

As described in Section 3.3, biotinylated streptavidin was deposited on commercial AAO substrates (with different pore diameters on either sample side: 177±20 nm and 29±7 nm respectively; uncoated or, coated with Au) and examined by fluorescence measurement as a function of sample orientation.

The deposited samples were mounted on a rotational stage and excited by a 10 mW 488 nm line of an Ar ion laser, which was further focused to a spot of 50 μm^2 by a 10 cm lens in a confocal configuration (Figure 3.7) An optical filter in front of the spectrometer (λ=495 nm) provided cutoff of the laser line. The scattered light (fluorescence signal) was collimated and focused onto the spectrometer slit. A PMT was used for detection. A typical fluorescence signal of biotinylated streptavidin is shown in Figure 4.1. The fluorescence signals decayed over time. This may be attributed to a competition between photobleaching [53] and recovery processes. In order to further investigate such a phenomenon, successive fluorescence scans such as shown in Figure 4.1 were taken at 5 minute intervals. The peak intensity for each of the scans always

stayed at λ=515 nm and is plotted in Figure 4.2. As seen by the least squares trend curve the signal mildly decays according to a power law, $\approx 1/\sqrt{t_n}$, where t_n is the time of the *n*th spectrum in a sequence. The fluorescence reaches quasi-steady-state conditions after approximately 1 h. Thus, in order to ensure a constant response, all the consequent data acquisitions were made after exposing the sample to 100 mW of laser intensity for 1 h.

Biotinylated lipid bilayers alone (i.e., without DTAF-streptavidin bound) did not exhibit any measurable fluorescence signals, as expected. AAO substrates were also exposed to DTAF-streptavidin aqueous solution at 30 °C following the same procedure as for aqueous lipid dispersion; namely, excess material was washed by buffer and the substrates were air dried. Figure 4.3 shows that such samples exhibit fluorescence signal similar to Figure 4.1 albeit a bit weaker than the biotinylated lipid/streptavidin complex. This demonstrates some nonspecific binding of DTAF-streptavidin to alumina surfaces in accord with previous observations [12]. The minute difference in the curve amplitudes is attributed to local fluctuations. The samples were not exposed to laser light prior to taking the data hence the relative large signals.

As mentioned above, we overcame the time dependent fluorescence signal issue by exposing the samples to laser radiation of 100 mW for 1 h prior to taking the data. Only then we conducted our measurements at 10 mW - one tenth of the initial laser intensity. Fluorescence signals were recorded as a function of incidence angle for two polarization states, either TE or TM-polarization, using a confocal arrangement with the help of a spectrometer and a photomultiplier (Figures 4.4(a) and (b)). Successive wavelength scans were made for each data point in order to determine the exact position of the fluorescence peak.

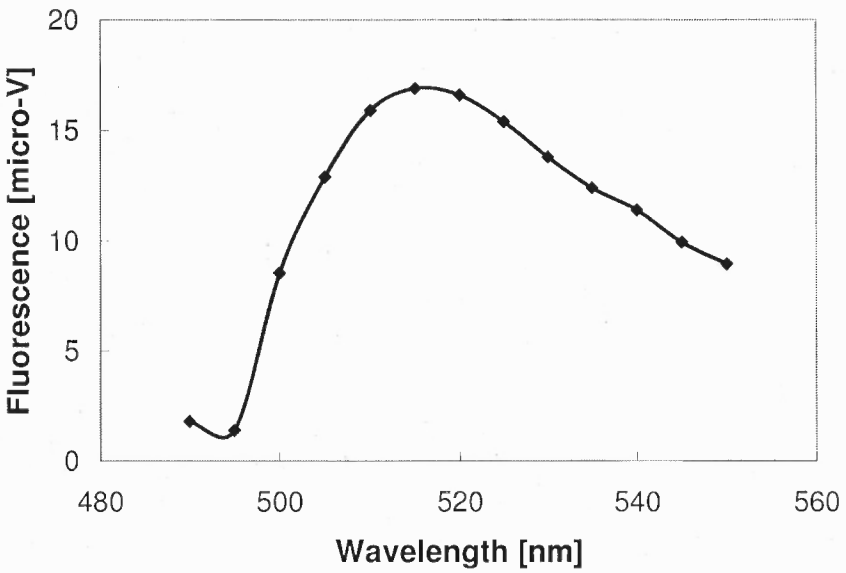

Figure 4.1 Fluorescence of biotin/streptavidin on a lipid bilayer within the pores of AAO. The laser intensity was 10 mW focused to a spot of 50 micron^2 by a 10 cm lens in a confocal configuration. An optical filter in front of the spectrometer (λ=495 nm) cut off the laser line.

In general, the intensity of the fluorescence peak is expected to be affected by individual hole geometry, the periodic pattern of the pores, and by surface plasmons, which are excited in the metal layer if the latter is present. A geometrical factor accounts for the orientation of the pores and macroscopic alignment (if any) of dipoles of the fluorescing chromophores with respect to the incident polarized beam. While surface plasmons may only be excited in metallic surfaces, surface waves may also exist in perforated dielectric films.

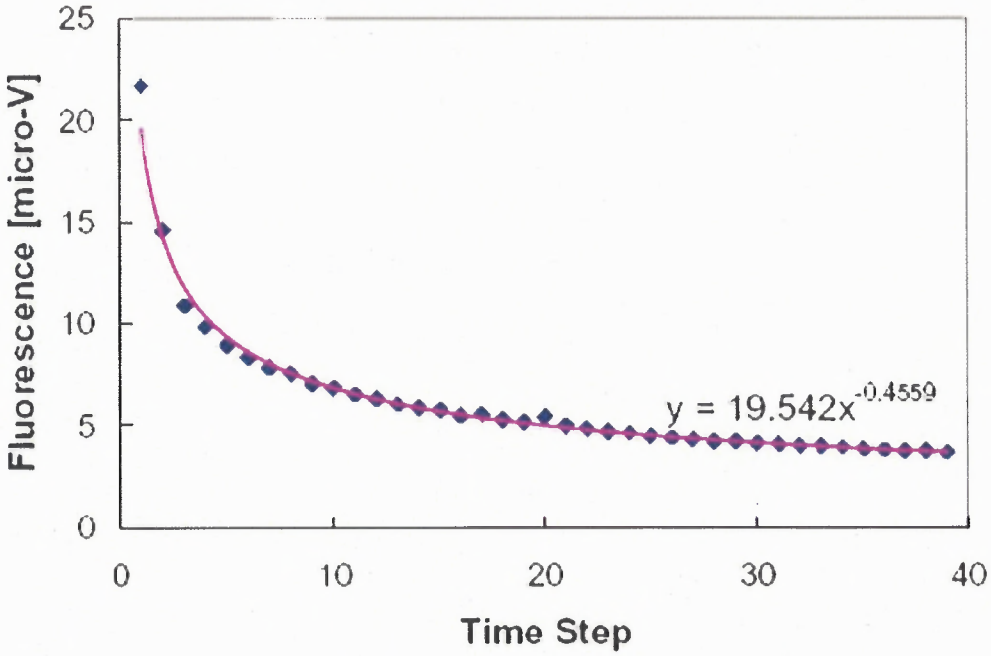

Figure 4.2 Fluorescence peak intensity as a function of time (filled diamond) and least squares fit to $\approx 1/\sqrt{t_n}$ (solid line)

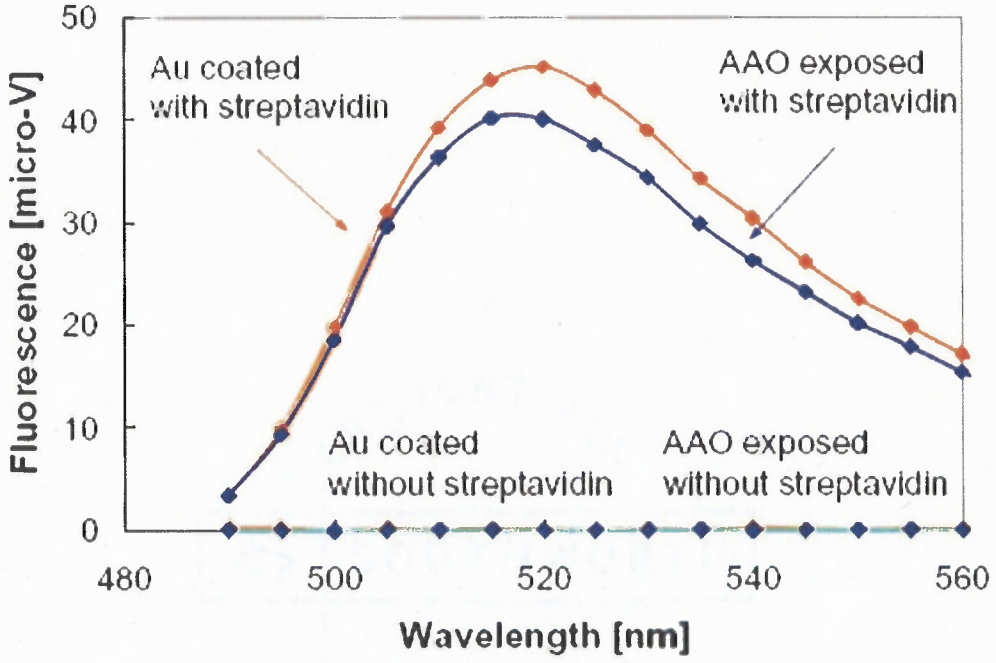

Figure 4.3 Fluorescence spectra of biotinylated lipid bilayers deposited into either exposed or Au coated AAO substrates before (filled diamonds) and 10 minutes after being introduced to the streptavidin. The samples were not exposed to the laser light prior to taking the data hence the relative large signal.

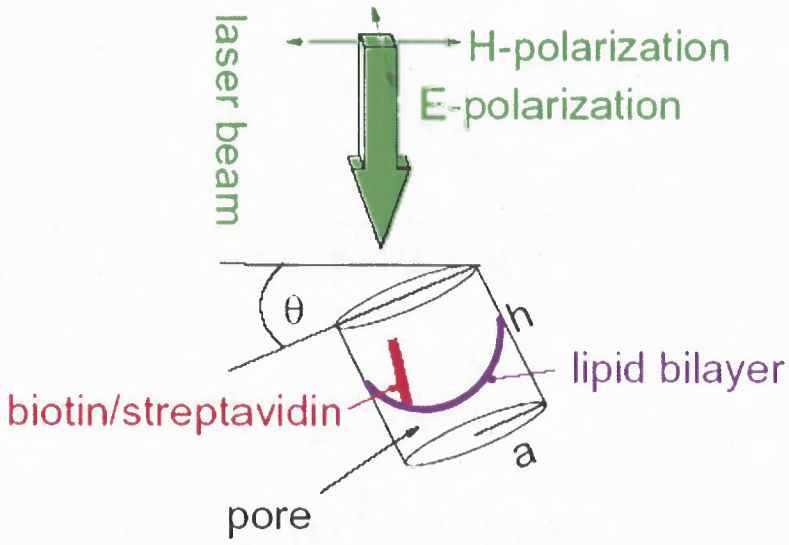

(a)

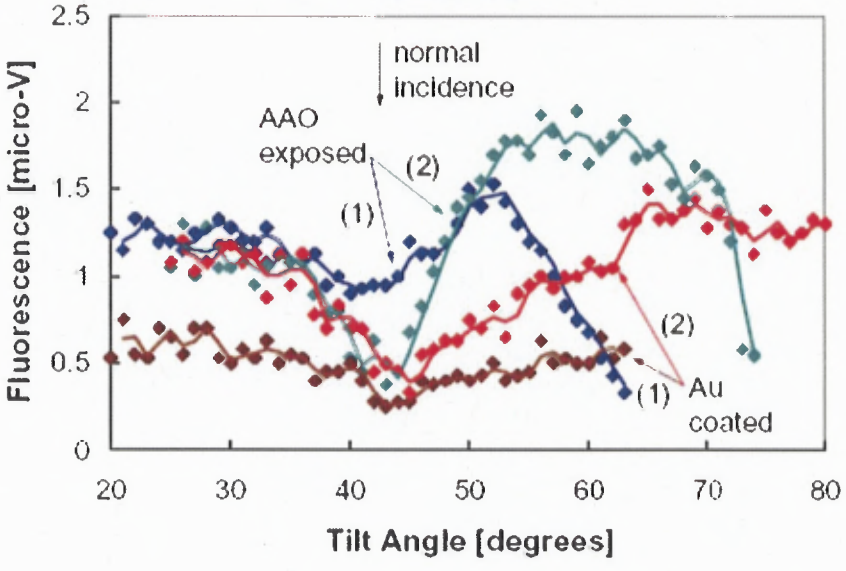

(b)

Figure 4.4 (a) Experimental configuration with marked *H*-and *E*-polarization modes. (b) Fluorescence peak intensity for *H*-polarized incident beam. Normal incidence position is at θ=43°.

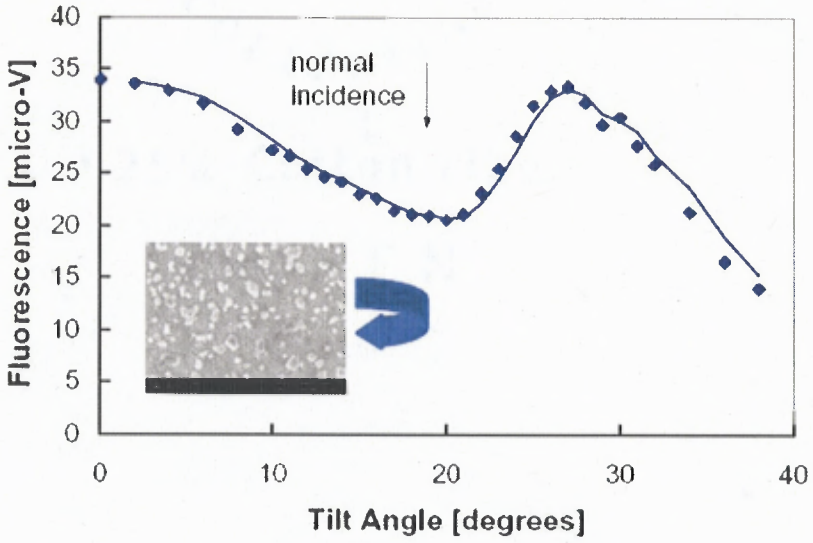

(c)

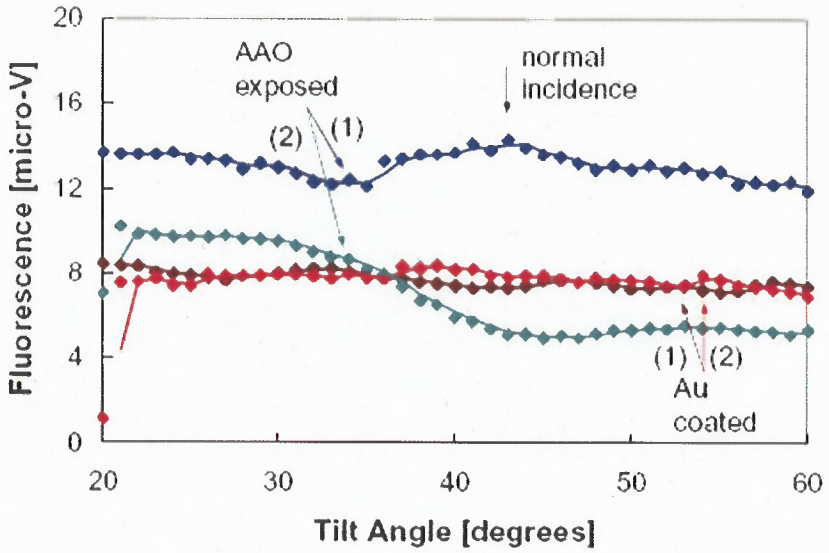

(d)

Figure **4.4 (c) Repeated experiments for exposed (uncoated) AAO substrate (1) after one month: the curve has the same extinction ratio $(I_{max}-I_{min})/I_{min}$, albeit with an overall intensity value differences. The inset indicates out-of-plane tilt. (d) The sample was rotated azimuthally (in-plane) rotation) by 90° and the experiments were repeated.**

4.1.2 Results

The effective area of a given pore, which is directly exposed to the laser beam, is a function of the tilt angle. On the other hand, if the dipole moment of streptavidin is aligned along the pore axis, the fluorescence due to the TE-polarization mode (*E*-polarization, *E*-pol; also denoted as s-pol by some; see Figure 4.4 (a) for definitions) is expected to be independent of the tilt angle. The excitation component, which is partially parallel to the biotin/streptavidin dipole moment, increases for the TM-polarization (*H*-polarization, *H*-pol; also known as *p*-pol by some) as the tilt angle increases. Such geometrical effects are expected to maximize the fluorescence peak for the *H*-pol state at some tilt angle. The peak fluorescence angle for the *E*-pol state would be at normal incidence.

The peak of the fluorescence signal as a function of the tilt angle θ for the *H*-polarized incident beam is shown in Figure 4.4. Clearly seen is a quasi symmetric curve for all the four AAO surfaces examined, with minima appearing at normal incidence. The experiment was repeated one month later with similar results (Figure 4.4(c)). When the sample was azimuthally rotated by 90° and assessed again with the *H*-polarized incident beam (Figure 4.4(d)), the response was basically flat for all of the surfaces except for the uncoated (exposed) AAO sample (2), which has the largest average pore diameter.

Figures 4.5 (a) and (b) exhibit fluorescence signal as a function of the tilt angle for the *E*-pol incident beam. In contrast to the *H*-pol incident beam results, a quasi flat response was observed for all of the four surfaces: a shallow dip whose position varied from sample to sample was sometimes observed (Figure 4.5). The experiment was repeated one month later with basically similar results (not shown). When the sample was

azimuthally rotated by 90° and assessed with *E*-pol incident beam, the response was yet again, quasi flat.

When a polarized light impinges on a sample at normal incidence its polarization state (the direction of electric field oscillations) is parallel to the substrate surface (not to be confused with the surface of the pores, which extend throughout the substrate). This holds true regardless of the *H*- or *E*-polarized mode used. We have monitored the peak intensity of the fluorescence signal as we rotated the sample azimuthally (in-plane rotations as indicated by the inset of Figure 4.6(a)) about its normal to the AAO surface (Figures 4.6(a) and (b)). As can be seen from the figures, the signal intensity oscillates with two periods: 240° and 120°. Such oscillations imply a crystallography effect by the hole array orientation on the fluorescence signal. The radial plot indicates asymmetry in the curve which is likely due to inhomogeneities in the sample as it is rotated about its normal axis. Nevertheless, the fluctuations in the curve upon rotating the sample by 360° are less than 10%. Notably, the observed angular period seems to be multiples of 60° but do not follow the C_6 symmetry exactly. We speculate that the main reason for this is local scatterings, which are due to the inhomogeneity of the hole array. Such scatterings are reduced somewhat when the surface of the sample is coated with a thin layer of Au (Figures 4.6(c) and (d)) probably because the electric field better confines to the sample surface.

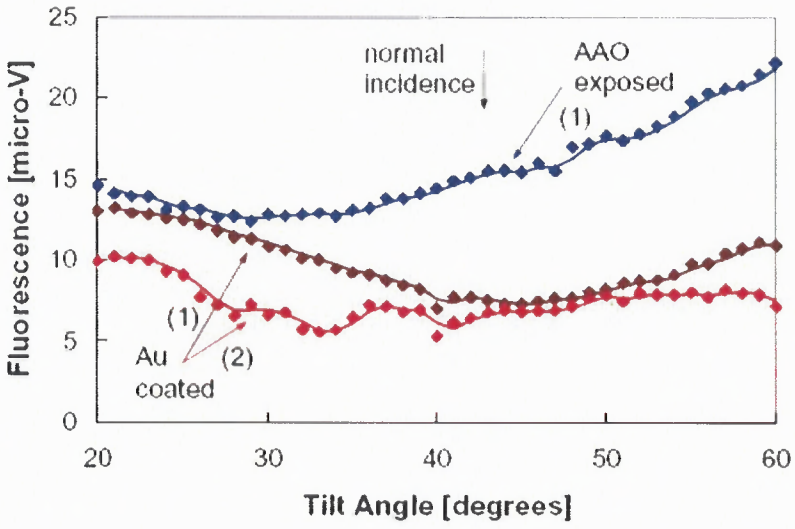

(a)

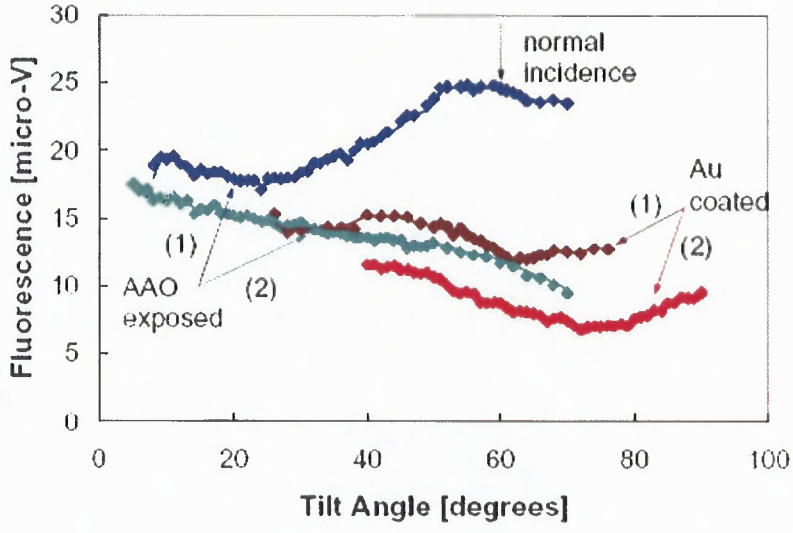

(b)

Figure 4.5 (a) Fluorescence peak intensity for *E*-polarized incident beam. Normal incidence position is at θ=43° with the exception of θ=40° for the exposed sample (1). (b) The samples were azimuthally rotated by 90° and the tilt experiments were repeated. Normal incidence position is at θ=60° with the exception of θ=43° for the exposed samples.

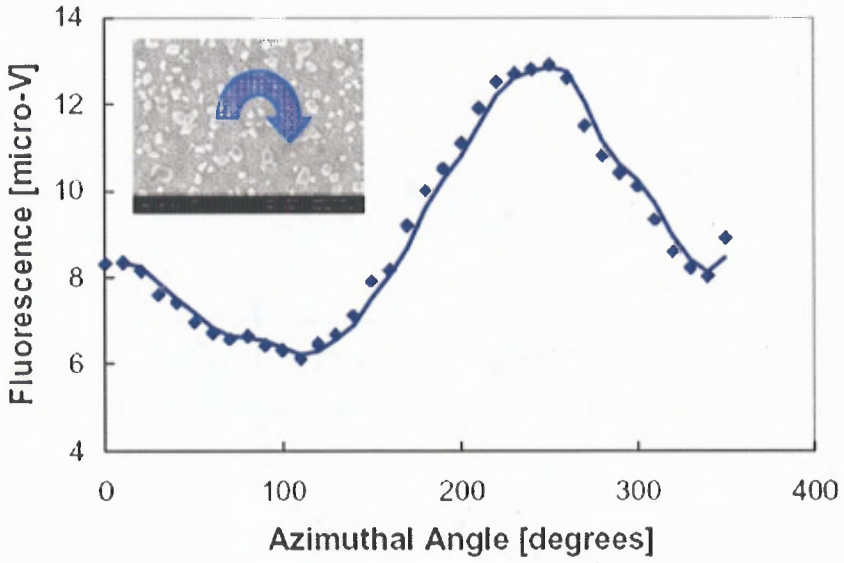

(a)

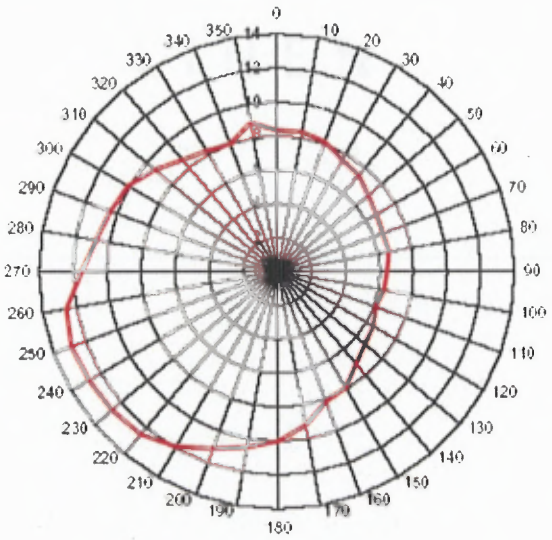

(b)

Figure 4.6 (a) Fluorescence peak intensity as a function of azimuthal angle (in-plane rotations as indicated by the inset) for the exposed (uncoated) sample (2) at normal incidence. (b) Radial plot: the asymmetry in the curve is likely due to sample inhomogeneities.

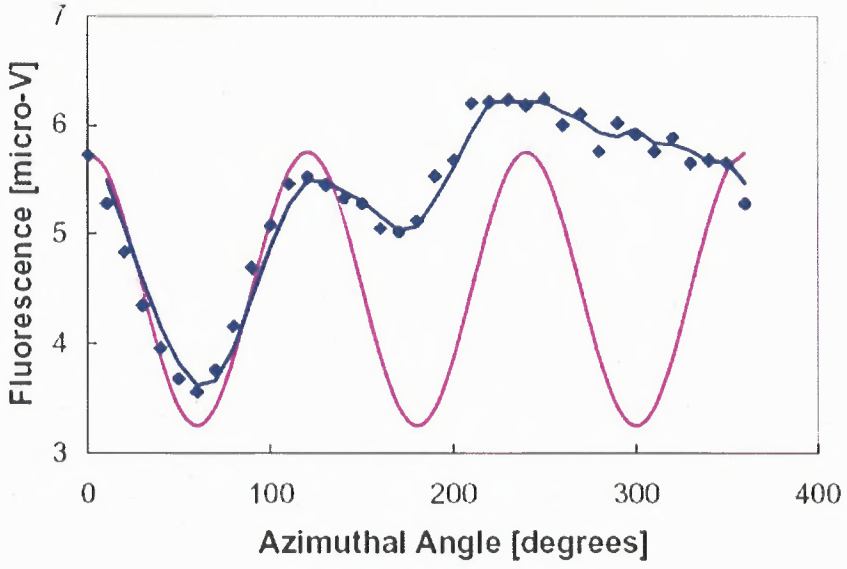

(c)

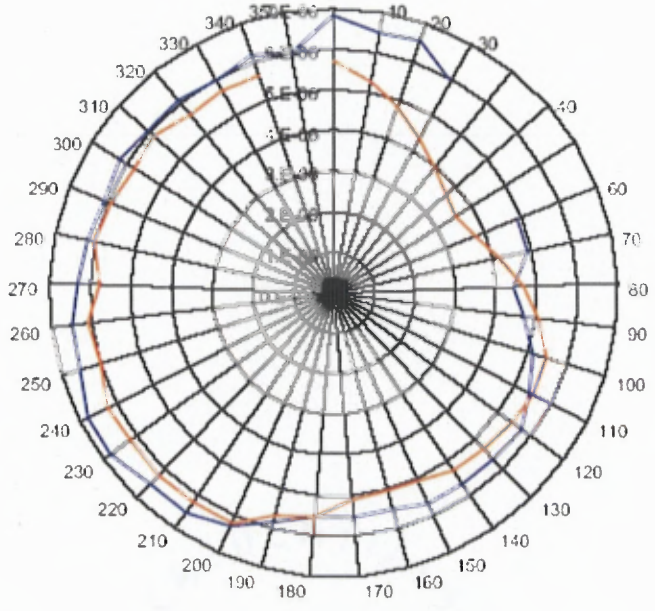

(d)

Figure 4.6(c) Fluorescence as a function of azimuthal angle for Au-coated sample (2) at normal incidence. The purple curve is a shifted sinusoidal curve indicating a threefold symmetry. (d) Repeated measurements demonstrate acceptable reproducibility for the radial plot.

Along the discussion in the Section 2.4, there are two major requirements for fluorescence signal enhancement: (i) an efficient coupling to a surface mode and (ii) a phase match condition with an appropriate crystallographic plane of holes (air rods). The first requirement dictates a proper tilt and azimuthal (in-plane rotation) angles such that the light is coupled by the first order of diffraction to a surface mode. If we treat the hole array as a grating with a given pitch, the efficiency of this coupling process may be approximated by $\sin^2(\Delta\eta/2)$, where $\Delta\eta$ is the phase difference between the grating and the propagating beam. The second requirement is related to a Bragg scattering between this surface mode and the array of holes when the beam propagates inside the AAO substrate. Such scattering is expected to be affected by only the azimuthal or in-plane rotation angle.

4.2 Fluorescence Enhancement of Dye Imbedded AAO

Here we extend our studies to include simple dye molecule (fluorescein) within in-house AAO samples. Our samples exhibited better crystallographic hole structure. In addition, the oxide layer is only 50 nm thick. Finally, the oxide layer is bound by a metal (aluminum). The substrates were prepared according to well-established recipe [34, 35] as described in Section 3.1.3.

The dye deposited nano-hole array sample was mounted on a rotational stage and excited by a 10 mW 488 nm or, the 514.5 nm lines of an Ar ion laser. The laser beam was further focused to a spot of 10 μm^2 by a lens in a confocal configuration (Figure 3.7). A low-pass optical filter in front of the spectrometer (λ=495 nm or =520 nm) was used in order to eliminate the related laser lines. The scattered light (the fluorescence signal) was

collimated and focused onto the spectrometer slit. A PMT was used for detection. A typical fluorescence signal of fluorescein is shown in Figure 4.7.

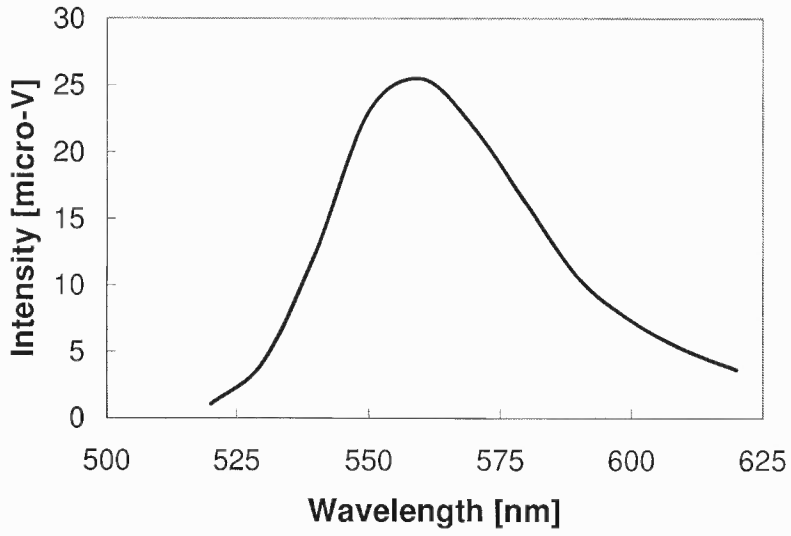

Figure 4.7 The Fluorescence signal of fluorescein.

As mentioned in previous Section 2.4, we expect 60° symmetry upon in-plane rotations for our hexagonal array of holes. When the wavelength is at resonance with a specific wavelength, such as occurs for the fluorescing wavelength at 560 nm, we expect 30° doubling symmetry upon in-plane rotations. Furthermore, if the platform is tilted at θ~9° efficient coupling to surface plasmons waves and enhanced fluorescence is expected.

In Figure 4.8 we show two examples of AAO substrates impregnated with fluorescein. As noted from Figure 4.7, the peak intensity is at λ=560 nm, within the transverse confinement of the hole-array. As the samples are rotated in-plane, a clear cycle appears. The cycle is of 30 degrees – double the hexagonal symmetry of the hole-array. Also provided in the figures are analytical curve of $sin^2(6\theta+\theta_0)$. A constant shift of θ_0 provides a match between the starting point of rotation and the unknown

crystallographic orientation of the hole-array. We postulate that the period doubling appears at transverse resonance, namely, when the transverse propagation mode is frustrated by the period or its sub-harmonics of the hole-array [33]. Unlike our previous examples (presented in Section 4.1), the pump wavelength is too far from the resonance to affect the fluorescence signal.

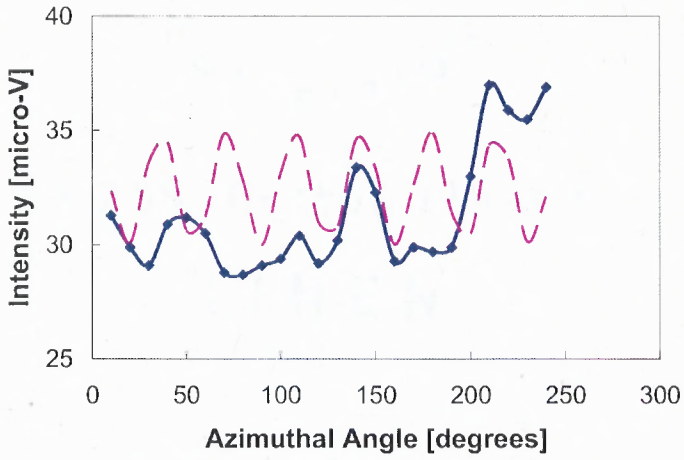

(a)

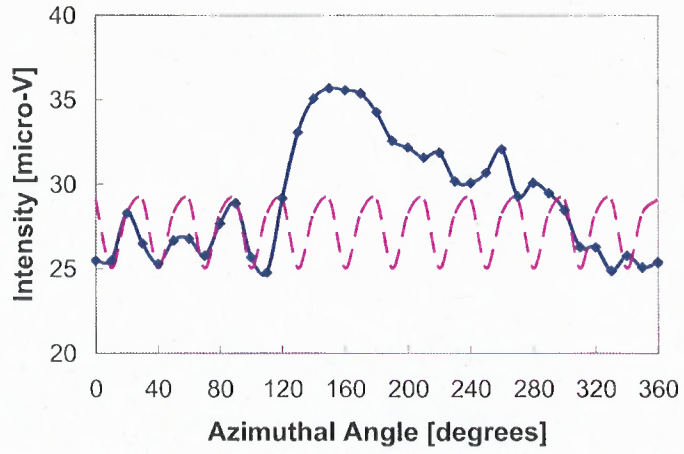

(b)

Figure 4.8 Fluorescence as a function of in-plane rotations (azimuthal angle) for normally incident, linearly polarized beam. (a) Sample 1 was exited with the 488 nm line of Ar laser. (b) Sample 2 was exited with the 514.5 nm line of Ar laser. The dash curve points to the oscillations of 30 degrees, $sin^2(6\theta+\theta_0)$, with θ_0 a constant shift. Note the loss of coherence after a few cycles due to existence of domains in the array of holes.

Another example is shown in Figure 4.9. The sample was pumped with the 514.5 nm line of Ar ion laser. As the sample was rotated azimuthally, its fluorescence characteristics resembled those of Figure 4.8 (b). The experiment was then repeated as a function of tilt angle. No special angular characteristics observed when the sample was pumped with TE incident mode – a mode for which the electric field is oscillating in parallel to the sample surface - the signal remained basically constant. However, when pumped with TM incident mode, there were marked signal variation at θ=8° and 12° as expected from Eq. (2.39).

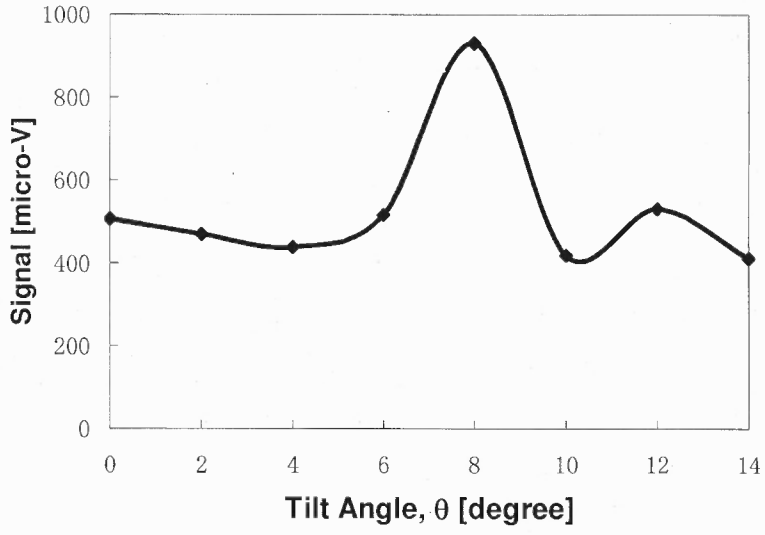

Figure 4.9 Fluorescence as a function of tilt angle for TM incident polarized beam. Note the enhanced fluorescence for tilt angles θ=8° and 12°.

4.3 Discussions

We set to investigate effects of polarized incident beams and sample orientation on chromophore bound AAO substrates. As for the first example, we studied the fluorescence signal of DTAF-conjugated streptavidin, which was bound to biotinilated

lipid bilayers. The latter were imbedded in nanopores of commercial anodized aluminum oxide platforms. The streptavidin was labeled with fluorescein, a chromophore marker. Our initial hypothesis was that the fluorescence signals from these chromophores will not be substantially affected by the orientation of the substrate, nor its pores, when pumped with various polarized incident beams. We varied the sample orientation with respect to the pumping optical beam in two ways: (i) by tilt angle θ—this was to test the effects of local chromophore orientation with respect to the polarized incident beam—and (ii) by in-plane rotations, or, azimuthal angle ϕ at normal incidence beam—this was to study the effect of the crystallographic hole-array orientation with respect to the beam's linear polarization state. Our hypothesis was proven wrong: unexpectedly, the experimental data demonstrated variations in the fluorescence signal both upon tilting the sample with respect to the beam direction and with respect to the azimuthal (in-plane) sample rotations.

In general, the larger signal variability was achieved with the *H*-polarization mode for a certain crystallographic sample orientation. The data for the *E*-polarized incident beam also exhibited some signal fluctuations as a function of tilt angle; yet, its extinction ratio $(I_{max}-I_{min}) / I_{min}$ was much smaller than the corresponding value for the *H*-polarized mode. In addition, no correlation between the position of the signal minima (whenever present) and approximate crystallographic orientation of the hole array could be established. We, therefore, hypothesize that the observed polarization effects may be attributed to the formation of selective light intensity distribution within the holes of the AAO substrates [4].

SEM images of these commercial AAO substrates revealed an imperfect pore homogeneity and packing. Nevertheless, polarization-dependent signal along certain crystallographic directions alludes to selective coupling between the fluorescence mode, which propagate in the AAO sample and the radiative modes (those modes are scattered back, propagate in free space, and detected by the spectrometer/detector system). Moreover, the clearer signal for Au-coated surfaces implies the role of surface plasmons in the coupling process [7].

The fluorescence signal exhibited a rather mild decay over time when exposed to prolonged irradiation of the laser light. Such decay behavior could be well fitted by a power law, $\approx 1/\sqrt{t_n}$ (solid line in Figure 4.2). In general, if the lifetime of the fluorescing molecule is relatively long, a steady state may be reached. For DTAF-streptavidin the half-lifetime value is about 16–21 second depending on the solvent [53]. On the other hand, if there is a feedback mechanism (such as arising from scattering by the array of holes), it is expected to impact the signal decay of such long-lived fluorescing molecules. Therefore, we may attribute the time dependent fluorescence signal to the additional scatterings by the porous platform besides the inherent photobleaching effect. Platforms built upon arrays with homogeneous and periodically packed nanopores ought to accentuate such behavior even further.

As for the other example, we used in-house substrates: here, the oxide layer was very thin (50 nm) on the top of the aluminum. Ordinary dye material (fluorescein) was utilized to study the effect of sample orientation with respect to the incident laser polarization. Similarly, the fluorescence signal exhibited strong dependence on the sample orientation: the signal increased by a factor of almost 2 when the sample was

tilted at an angle of 8 degree compared to the signal for the normal incidence condition. In addition, as the sample was rotated in-plane (azimuthally), the fluorescence signal exhibited oscillations of 30 degrees. The reason here is that the fluorescence wavelength is commensurate with the symmetry of the sub-wavelength hole-array and hence exhibits period doubling.

4.4 Conclusions

An analytical methodology has been introduced here to enhance fluorescence signals from bio-species by nanoporous aluminum oxide substrate. Specifically, it was found that a model protein-lipid bilayer complex, formed upon noncovalent binding of DTAF-conjugated streptavidin to biotinylated lipid bilayers and deposited into a nanoporous array in anodized aluminum oxide films, exhibited different fluorescence characteristics for *E*-polarized and *H*-polarized incident optical beams. Variations in the fluorescence signals in the presence of a thin coating of gold on the sample surface were also observed. The origin of the observed polarization-dependent effects could be explained by a simplified model which assumed a macroscopic alignment of the fluorescing dipole with respect to the oscillating pumping electric field. The effect of linearly polarized incident beams on the fluorescence of dye imbedded, 2-D photonic crystals with array of nano-holes was examined as well. Marked signal variations were observed at specific platform orientations (achieved by tilting or, in-plane rotations of the sample), which could be understood as arising from local resonating effects. Understanding the mechanisms of such behavior may assist us in designing better platforms for biochemical detection and further development of this analytical tool.

CHAPTER 5

GAIN AND LINEWIDTH NARROWING IN PLASMONIC WAVEGUIDES

In this chapter, we demonstrated a gain of 3 and 30% linewidth narrowing in plasmonic waveguides. Gain was provided by a dye imbedded in the structure's pores. Feedback for the fluorescence signal was provided by the sub-wavelength hexagonal hole-array in the oxide layer.

5.1 System Configuration

As we discussed in Section 2.2, surface plasmons are near-field phenomena. Lasing requires gain and feedback; however, surface plasmons may experience large loss as a result of currents, induced in the conductor(s). In order to study gain and feedback in plasmonic waveguides we offer the following approach. We examined surface waveguides in which a perforated thin oxide layer on top of a metal substrate (Figure 5.1). Gain was provided by dye s (fluorescein) imbedded in a perforated oxide material (alumina) or, by defect states in the oxide layer, unlike the approach suggested in [54] or, in [55]. The feedback was provided to the SP waves by periodic hole-array, similarly to the construction of photonic crystal for semiconductor lasers [56, 57]. Dispersion of SP waves in a TM mode contains two branches whose frequency separation defines an energy gap [58]. Thus in principle, light may be pumped through one band edge and the scattered light may escape from the other. While periodic structures, which confine SP waves in the long-wavelength regime, have been known for years [58-60] we operate in

the very long wavelength regime: the pitch of the periodic structure is much smaller than the incident wave length and is realized in AAO films [4, 6].

Let us consider an ideal 2D hexagonal case, which is similar with the model in Section 2.4 (Figure 2.7). Suppose that the surface component of the wave inside the AAO sample is scattered from the same periodic structure as we defined before. This may happen because the AAO is made of densely packed holes with inter hole-spacing much smaller than the propagating wavelength. This is also happening because of the abrupt nature of the hole in the AAO slab, invoking higher-orders and sub-orders of diffraction. One can envision that such Bragg diffraction creates a standing wave within the hole-array. These considerations are true for the pump as well as, for the fluorescing wavelengths.

There are two frequencies associated with a given launching angle θ: these are ω^- and ω^+ corresponding to $\boldsymbol{\beta}^-$and $\boldsymbol{\beta}^+$, respectively. The difference frequency, $\delta\Omega=\omega^+-\omega^-$ defines a frequency gap. We note that $\boldsymbol{\beta}^+-\boldsymbol{\beta}^-=2qG$, therefore, a larger coupling is expected between the corresponding frequencies. At normal incidence, $\theta=0$, the incident beam generates two counter-propagating surface waves (a standing wave) $\beta=\pm qG$ and the gap closes. Optimal fluorescence conditions occur when the mode propagating along the surface is a standing wave and coupled by the periodic structure.

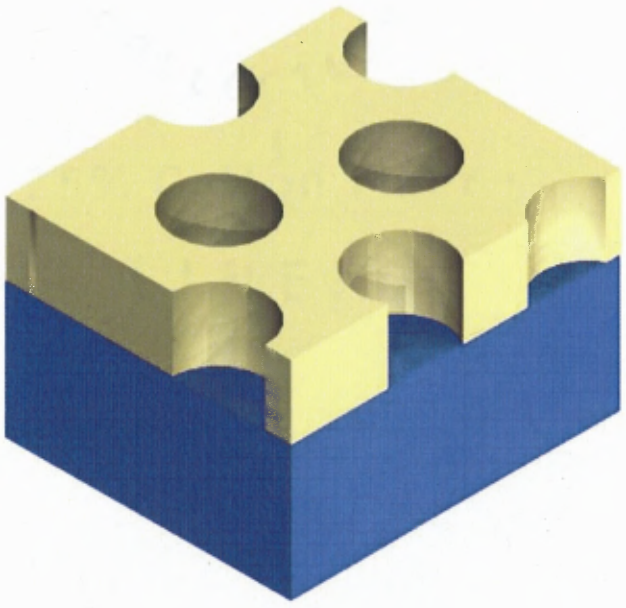

(a)

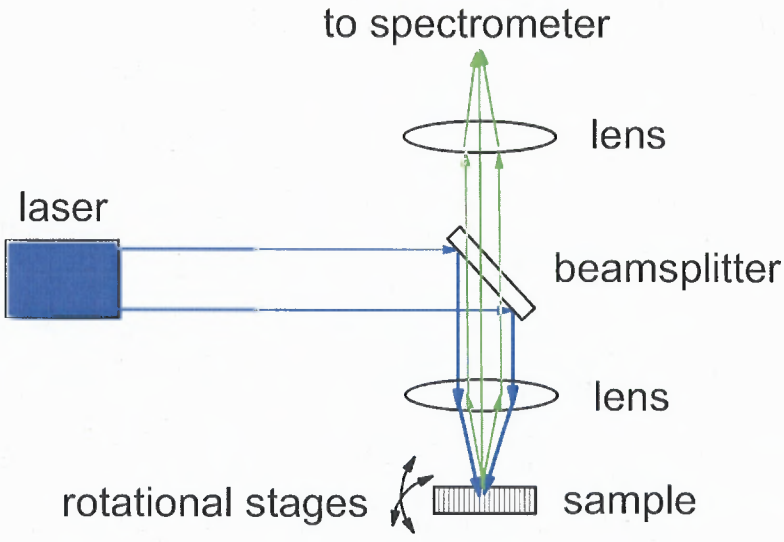

(b)

Figure 5.1 (a) Hole-array in alumina (pale yellow) on aluminum (blue); (b) Experimental configuration. We used a x10 objective lens to focus the Ar laser beam onto the sample; when using the Nd: YAG laser the lens had a 5 cm focusing distance. The lens focusing the fluorescence onto the spectrometer slit had *f*=10 cm in all cases.

Since we are dealing with sub-harmonics, Eq. (2.38) predicts transverse resonance effect at normal incidence for λ~556 nm with a~90 nm; $n_{eff} = \sqrt{\varepsilon_1 \varepsilon_2 / (\varepsilon_1 + \varepsilon_2)}$ ~1.02; q_1=1/7, q_2=0. It also predicts a resonance at λ=636 nm with q_1=1/8, q_2=0. Optimal conditions may be achieved by a small tilt and in-plane rotation of the sample with respect to the incident beam due to the incomplete gap throughout the Brillouin zone for the hole-array (as discussed in Sec 2.4). For example, Eq. (2.39) predicts θ= 4.7° and θ= 8.9° with q_2=0; q_1=1/6 for the pump wavelength at 514.5 nm and the 550 nm fluorescence line, respectively. It predicts θ = 4.1° for the 680 nm fluorescence line of the AAO with q_2=0; q_1=1/8. A standing wave for the 550 nm line occurs approximately with q_2=1/10; q_1=-1/10. In fact, one may find numerous resonances in the range between 5-12 degrees because of the densely packed hole-array structure. Added to that is a fairly wide resonance condition due to local scatterings. Finally, we note for the AAO that the strongest electric field is within the holes, at the air/oxide interface level [4].

In the experiments, we used a confocal arrangement whereby the sample was tilted and azimuthally rotated (in-plane rotations) with respect the linearly polarized incident beam until optimal conditions for launching the SP waves have been reached. In-plane rotations were needed due to the incomplete frequency gap. Experimentally, we found that the best tilt angle for fluorescence purposes with the dye material was θ~8°, fairly close to the θ=9° predicted above. This also corroborated previous results with Raman spectroscopy [4]. As mentioned before, the samples were made of anodized aluminum oxide (AAO). The 50 nm thick oxide layer, perforated with a hexagonal hole-array was lying on top of aluminum substrate.

5.2 Results and Discussions

Fluorescence as a function of wavelength is shown in Figure 5.2 for samples pumped with Ar ion laser at 514.5 nm. Upon increase of the intensity, samples exhibited a fluorescence peak shift from 560 nm towards 550 nm (Figure 5.2(b)). This is due to the diminishing effect of longer fluorescing wavelengths by the confining periodic matrix. A careful examination of the fluorescence peaks as a function of pump intensity reveals a 3 nm linewidth broadening for the AAO samples. The intensity curve (Figure 5.2(b)) exhibited some undulations, which may be the result of lock-in phase fluctuations.

These data triggered us to use a pulse laser (double frequency, Nd:YAG laser, 10 nano-seconds pulse at 532 nm) as well. As seen from Figure 5.3, a gain of 3 is noted from the curve: as the input pump intensity increased by a factor of approximately 2, the fluorescence signal at 550 nm increased by a factor of 6. At the same time, the linewidth of the fluorescence reduced from 35 nm to 24 nm – approximately a 30% reduction.

Fluorescence is also observed, around 680 nm. The line is attributed to the defect states in the oxide layer (AAO). Here we observe no linewidth narrowing for the AAO substrates. Larger enhancement and linewidth-narrowing of the 680 nm line may be achieved by proper tilt and in-plane rotation of the samples.

5.3 Conclusion

In summary, gain and linewidth narrowing have been demonstrated for periodic, sub-wavelength structures, which support surface plasmons. Such construction may open the door for new bio-chemical applications, bringing the source of interrogation closer to the molecules under test.

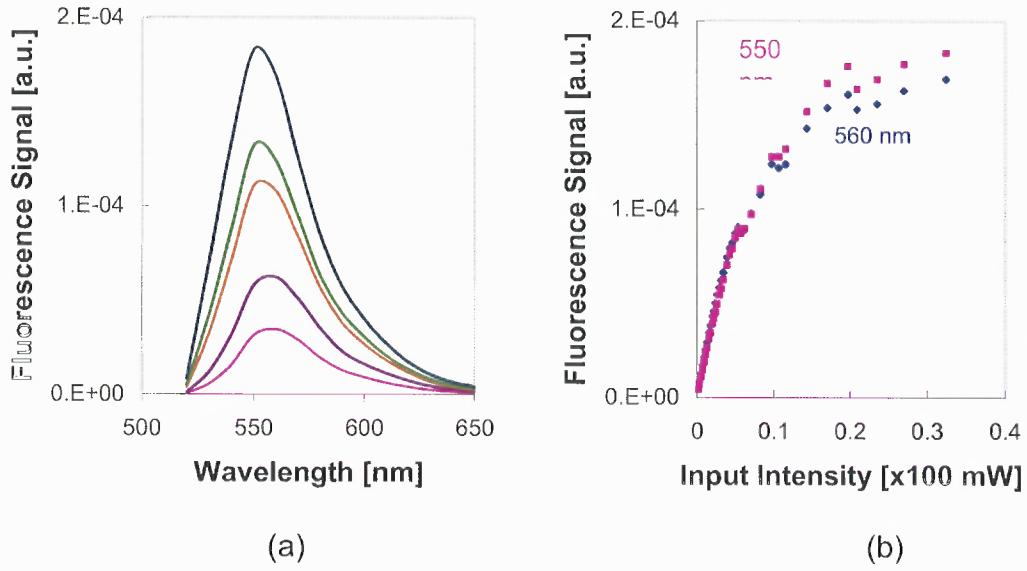

Figure 5.2 Pumped with Ar laser: (a) Fluorescence as a function of wavelength. (b) Fluorescence as a function of input intensity. The linewidth broadened by 3 nm for the unbounded SP mode as the intensity of the pump laser increased.

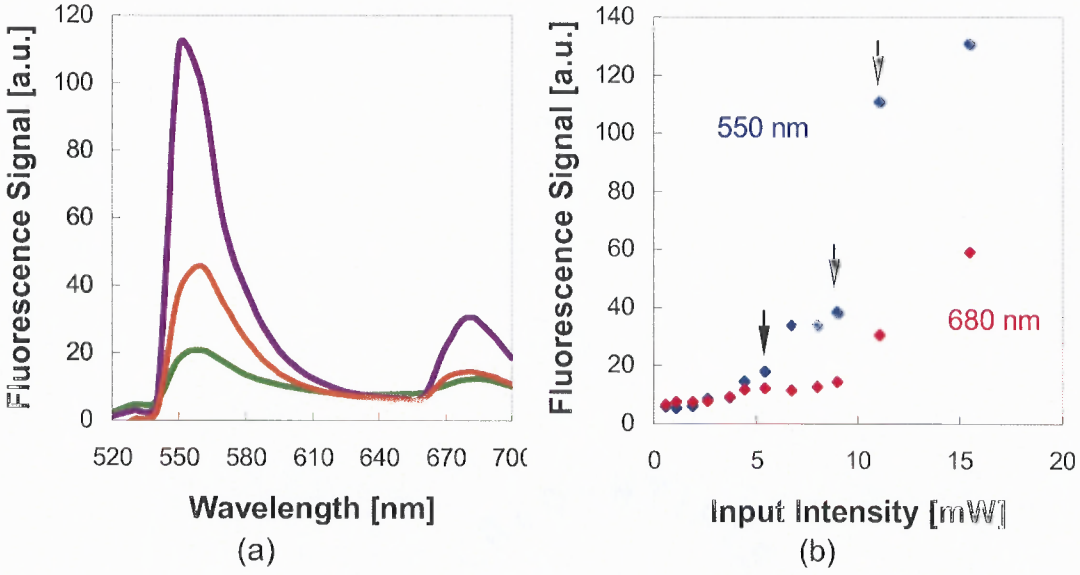

Figure 5.3 Pumped with Nd:YAG laser: (a) Fluorescence as a function of wavelength. (b) Fluorescence as a function of input intensity. The arrows mark the curves in (a). The linewidth has narrowed by 11 nm. The linewidth remained constant for the AAO defect line at 680 nm.

CHAPTER 6

CONCLUSION AND FUTURE WORK

6.1 Conclusion

In our study, novel applications of AAO films as a signal enhancing platforms for fluorescence signals have been investigated. We have presented a few examples: in one example we examined the effect of hole-array crystallography on the fluorescence signal of proteins bound lipid bilayer. It was found that such fluorescence signals depend upon the orientation of the AAO substrate when illuminated with *H*-polarized (*H*-pol or *p*-polarized) incident optical beams. On the other hand, the signal was almost constant when pumping with *E*-polarized incident beams. The origin of the observed polarization-dependent effects could be explained by assuming a macroscopic alignment of the fluorescing dipole with respect to the oscillating pumping electric field. Understanding the mechanisms of such characteristics may assist us in designing better platforms for biochemical detection and further development of this analytical tool. In the other example, the effect of in-plane sample rotations on the fluorescing signal was understood as resulting from local feedback by the array of holes. Finally, gain and linewidth narrowing in AAO bound plasmonic waveguides has been verified for periodic, sub-wavelength structures, which support surface plasmons. Such construction may open the door for new bio-chemical applications, bringing the source of interrogation closer to the molecules under test.

6.2 Suggestion for Future Work

Further optimization of these nano-structured platforms may be achieved through simulations in comparison with experimental data. Extending these findings to other macro molecules is also desired.

REFERENCES

[1] R. E. Ricker, A. E. Miller, and D.-F. Yue, "Nanofabrication of a Quantum Dot Array: Atomic Force Microscopy of Electropolished Aluminum," *Journal of Electronic Materials,* vol. 25, pp. 1585-1592, 1996.

[2] H. Masuda, M. Ohya, H. Asoh, and K. Nishio, "Photonic Band Gap in Naturally Occurring Ordered Anodic Porous Alumina," *Japanese Journal of Applied Physics,* vol. 40, pp. L1217-L1219, 2001.

[3] M. Sun, G. Zangari, M. Shamsuzzoha, and R. M. Metzger, "Electrodeposition of Highly Uniform Magnetic Nanoparticle Arays in Ordered Alumite," *Applied Physcal Letters,* vol. 78, pp. 2964-2966, 2001.

[4] C. Zhang, K. Abdijalilov, and H. Grebel, "Surface Enhanced Raman with Anodized Aluminum Oxide Films," *Journal of Chemical Physics,* vol. 127, pp. 044701, 2007.

[5] C. Zhang, A. Smirnov, D. Hahn, and H. Grebel, "Surface Enhanced Raman Scattering of Biospecies on Anodized Aluminum Oxide Films," *Chemical Physics Letters,* vol. 440, pp. 239-243, 2007.

[6] R.-Q. Li, A. Marek, A. I. Smirnov, and H. Grebel, "Polarization-dependent Fluorescence of Proteins Bound to Nanopore-confined Lipid Bilayers," *Journal of Chemical Physics,* vol. 129, p. 095102, 2008.

[7] H. Grebel, Z. Iqbalb, and A. Lana, "Detecting Single-Wall Carbon Nanotubes with Surface-enhanced Raman Scattering from Metal-coated Periodic Structures," *Chemical Physics Letters,* vol. 348, pp. 203-208, 2001.

[8] K. Kneipp, H. Kneipp, I. Itzkan, R. R. Dasari, and M. S. Feld, "Surface-enhanced Raman Scattering and Biophysics," *Journal of Physics: Condensed Matter,* vol. 14, pp. R597-R624, 2002.

[9] S. Sanchez-Cortes, R. Berenguel, A. Madejón, and M. Pérez-Méndez, "Adsorption of Polyethyleneimine on Silver Nanoparticles and Its Interaction with a Plasmid DNA: a Surface-enhanced Raman Scattering Study," *Biomacromolecules,* vol. 3(4), pp. 655-660, 2002.

[10] R. Langer and J. P. Vacanti, "Tissue Engineering," *Science,* vol. 260, pp. 920-026, 1993.

[11] A. I. Smirnov and O. G. Poluektov, "Substrate-Supported Lipid Nanotube Arrays," *Journal of the American Chemical Society*, vol. 125, pp. 8434-8435, 2003.

[12] A. M. Alaouie and A. I. Smirnov, "Formation of a Ripple Phase in Nanotubular Dimyristoylphosphatidylcholine Bilayers Confined Inside Nanoporous Aluminum Oxide Substrates Observed by DSC, " *Langmuir,* vol. 22, pp. 5563-5565, 2006.

[13] E. Y. Chekmenev, P. L. Gor'kov, T. A. Cross, A. M. Alaouie, and A. I. Smirnov, "Flow-Through Lipid Nanotube Arrays for Structure-Function Studies of Membrane Proteins by Solid-State NMR Spectroscopy, " *Biophysical Journal,* vol. 91, pp. 2976, 2006.

[14] R. C. Furneaux, W. R. Rigby, and A. P. Davidson, "The Formation of Controlled-porosity Membranes from Anodically Oxidized Aluminium," *Nature,* vol. 337, pp. 147-149, 1989.

[15] C. A. Foss, G. L. Hornyak, J. A. Stockert, and C. R. Martin, "Template-Synthesized Nanoscopic Gold Particles: Optical Spectra and the Effects of Particle Size and Shape," *Journal of Physical Chemistry,* vol. 98, pp. 2963 - 2971, 1994.

[16] D. Routkevitch, T. L. Haslett, L. Ryan, T. Bigioni, C. Douketis, and M.Moskovits, "Synthesis and Resonance Raman Spectroscopy of CdS Nano-wire Arrays," *Chemical Physics,* vol. 210, pp. 343-352, 1996.

[17] J. Homola, S. S. Yee, and G. Gauglitz, "Surface Plasmon Resonance Sensors: Review," *Sensors and Actuators, B: Chemical,* vol. 54, pp. 3-15, 1999.

[18] Y. Sun and Y. Xia, "Increased Sensitivity of Surface Plasmons Resonance of Gold Nanoshells Compared to That of Gold Solid Colloids in Response to Environmental Changes," *Analytical Chemistry,* vol. 74, 2002.

[19] C. R. Yonzon, J. Eunhee, S. Zou, S. George, C. M. Milan, and V. D. Richard, "A Comparative Analysis of Localized and Propagating Surface Plasmon Resonance Sensors: the Binding of Concanavalin A to a Monosaccharide Functionalized Self-assembled Monolayer," *Journal of the American Chemical Society,* vol. 126, pp. 12669-12676, 2004.

[20] T. Rindzevicius, Y. Alaverdyan, A. Dahlin, F. Höök, D. S. Sutherland, and M. Käll, "Plasmonic Sensing Characteristics of Single Nanometric Holes," *Nano Letters,* vol. 5, pp. 2335-2339, 2005.

[21] L. J. Sherry, S.-H. Chang, G. C. Schatz, and R. P. V. Duyne, "Localized Surface Plasmon Resonances: Spectroscopy of Single Silver Nanocubes," *Nano Letters,* vol. 5, pp. 2034-2038, 2005.

[22] Q. Xu, J. Bao, F. Capasso, and M. Whitesides, "Surface Plasmons Resonances of Free-standing Gold Nanowires Fabricated by Nanoskiving," *Angewandte Chemie International Edition,* vol. 45, pp. 3631-3635, 2006.

[23] M. E. Stewart, N. H. Mack, V. Malyarchuk, J. A. N. T. Soares, T.-W. Lee, S. K. Gray, R. G. Nuzzo, and J. A. Rogers, "Quantitative Multispectral Biosensing and 1D Imaging using Quasi-3D Plasmonic Crystals," *PNAS,* vol. 103, pp. 17143-17148, 2006.

[24] J. R. Fritz, E. B. Cooper, S. Gaudet, P. K. Sorger, and S. R. Manalis, "Electronic Detection of DNA by Its Intrinsic Molecular Charge," *PNAS,* vol. 99, pp. 14142-14146, 2002.

[25] E. Gorodkiewicz, A. Fernández-González, A. Akkoyun, G. Steiner, and R. Salzer, "Electronic Detection of Systematic Evaluation of A Surface Plasmon Resonance Imaging Biochip Reader: Study of Gold Surface Modifications," *Chemical Physics,* vol. 50, pp. 103-116, 2005.

[26] M. Born and E. Wolf, *Principles of Optics: Electromagnetic Theory of Propagation, Interference and Diffraction of Light.* New York: Cambridge University Press, 1999.

[27] H. Raether, *Surface Plasmons on Smooth and Rough Surfaces and on Gratings.* Berlin: Springer-Verlag, 1988.

[28] B. J. Munk, *Frequency Selective Surfaces.* New York: John Wiley & Sons, Inc., 2000.

[29] A. V. Akimov, A. Mukherjee, C. L. Yu, D. E. Chang, A. S. Zibrov, P. R. Hemmer, H. Park, and M. D. Lukin, "Generation of Single Optical Plasmons in Metallic Nanowires Coupled to Quantum Dots," *Nature,* vol. 450, pp. 402-406, 2007.

[30] J. R. Sambles, G. W. Bradbery, and F. Z. Yang, "Optical-excitation of Surface-Plasmons: An Introduction," *Contemporary Physics,* vol. 32, pp. 173-183, 1991.

[31] E. Yablonovitch, "Photonic Band Structure: the Face-Centered-Cubic Case," *Physical Review Letters,* vol. 63, pp. 1950-1953, 1989.

[32] J. M. Tobias and H. Grebel, "Self-imaging in Photonic Crystals in a Sub-wavelength Range," *Optics Letters,* vol. 24, pp. 1660-1662, 1999.

[33] J. M. Tobias, M. Ajgaonkar, and H. Grebel, "Morphology-dependent Transmission through Photonic Crystals," *Journal of the Optical Society of America (JOSA) B,* vol. 19, pp. 285-291, 2002.

[34] J. W. Diggle, T. C. Downie, and C. W. Goulding, "Anodic Oxide Films on Aluminum," Ch*emical Reviews,* vol. 69, pp. 365-405, 1969.

[35] H. Masuda and K. Fukuda, "Ordered Metal Nanohole Arrays Made by a Two-Step Replication of Honeycomb Structures of Anodic Alumina," *Science,* vol. 268, pp. 1466-1468, 1995.

[36] J. P. O'Sullivan and G. C. Wood, "The Morphology and Mechanism of Formation of Porous Anodic Films on Aluminum," in *Proceedings of the Royal Society of London. Series A, Mathematical and Physical Sciences*, pp. 511-543, 1970.

[37] J. Siejka and C. Ortega, "An O^{18} Study of Field-Assisted Pore Formation in Compact Anodic Oxide Films on Aluminum," *Journal of the Electrochemical Society,* vol. 124, pp. 883-891, 1977.

[38] Y. Xu, G. E. Thompson, and G. C. Wood, "Mechanism of Anodic Film Growth on Aluminum " *Transactions of the Institute of Metal Finishing,* vol. 63, pp. 98-103, 1985.

[39] K. Shimizu, K. Kobayashi, G. E. Thompson, and G. C. Wood, "Development of Porous Anodic Films on Aluminium," *Philosophical Magazine A,* vol. 66, pp. 643-652, 1992.

[40] K. Eblihara, H. Takahashi, and M. Nagayama, "Structure and Density of Anodic Oxide Films Formed on Aluminium in Oxalic Acid Solution," *Journal of the Surface Finishing Society of Japan,* vol. 34, p. 548, 1983.

[41] J. D. Joannopoulos, R. D. Meade, and J. N. Winn, *Photonic Crystals: Molding the Flow of Light.* Priceton: Princeton Univiversity Press, 1995.

[42] M. Wilchek and E. A. Bayer, "Methods in Enzymology," vol. 184 San Diego: Academic Press, 1990.

[43] M. Fleischmann, P. J. Hendra, and A. J. McQuillan, "Raman Spectra of Pyridine Adsorbed at A Silver Electrode," *Chemical Physics Letters,* vol. 26, pp. 163-166, 1974.

[44] "Protein Microarray Technology," D. Kambhampati, Ed. Weinheim: Wiley, 2004.

[45] C. Bieri, O. P. Ernst, S. Heyse, K. P. Hofmann, and H. Vogel, "Micropatterned Immobilization of A G Protein-coupled Receptor and Direct Detection of G Protein Activation," *Nature Biotechnology,* vol. 17, pp. 1105-1108, 1999.

[46] Y. Fang, A. G. Frutos, and J. Lahiri, "Membrane Protein Microarrays," *Journal of the American Chemical Society,* vol. 124, pp. 2394-2395, 2002.

[47] Y. Hong, B. L. Webb, H. Su, E. J. Mozdy, Y. Fang, Q. Wu, L. Liu, J. Beck, A. M. Ferrie, S. Raghavan, J. Mauro, A. Carre, D. Müeller, F. Lai, B. Rasnow, M. Johnson, H. Min, J. Salon, and J. Lahiri, "Functional GPCR Microarrays," *Journal of the American Chemical Society,* vol. 127, pp. 15350-15351, 2005.

[48] G. A. Lorigan, P. C. Dave, E. K. Tiburu, K. Damodaran, S. Abu-Baker, E. S. Karp, W. J. Gibbons, and R. E. Minto, "Solid-State NMR Spectroscopic Studies of an Integral Membrane Protein Inserted into Aligned Phospholipid Bilayer Nanotube Arrays," *Journal of the American Chemical Society,* vol. 126, pp. 9504-9505, 2004.

[49] E. Y. Chekmenev, J. Hu, P. L. Gor'kov, W. W. Brey, T. A. Cross, A. Ruuge, and A. I. Smirnov, "^{15}N and ^{31}P Solid-state NMR Study of Transmembrane Domain Alignment of M2 Protein of Influenza A Virus in Hydrated Cylindrical Lipid Bilayers Confined to Anodic Aluminum Oxide Nanopores," *Journal of Magnetic Resonance,* vol. 173, pp. 322-327, 2005.

[50] O. Fliniaux, C. Elie-Caille, J. Pantigny, and C. Bourdillon, "Production of Microporous Aluminum Oxide Electrodes as Supports for Tethered Lipid Bilayers of Large Surface Area," *Electrochemistry Communications,* vol. 7, pp. 697-702, 2005.

[51] O. Soubias, I. V. Polozov, W. E. Teague, A. A. Yeliseev, and K. Gawrisch, "Functional Reconstitution of Rhodopsin into Tubular Lipid Bilayers Supported by Nanoporous Media," *Biochemistry,* vol. 45, pp. 15583-15590, 2006.

[52] S. Cloutier, A. Lazareck, and J. Xu, "Detection of Nano-confined DNA using Surface-Plasmon Enhanced Fluorescence," *Applied Physics Letters,* vol. 88, p. 013904, 2006.

[53] M. Benchaib, R. Delorme, M. Pluvinage, P. A. Bryon, and C. Souchier, "Evaluation of Five Green Fluorescence-emitting Streptavidin-conjugated Fluorochromes for Use in Immunofluorescence Microscopy," *Histochemistry and Cell Biology,* vol. 106, pp. 253-256, 1996.

[54] D. J. Bergman and M. I. Stockman, "Surface Plasmon Amplification by Stimulated Emission of Radiation: Quantum Generation of Coherent Surface Plasmons in Nanosystems," *Physical Review Letters,* vol. 90, p. 027402, 2003.

[55] M. A. Noginov, G. Zhu, M. Bahoura, J. Adegoke, C. Small, B. A. Ritzo, V. P. Drachev, and V.M. Shalaev, Appl. Phys. B, 86, 455–460 (2007), "The Effect of Gain and Absorption on Surface Plasmons in Metal Nanoparticles," *Applied Physics B,* vol. 86, pp. 455-460, 2007.

[56] S. Noda, M. Yokoyama, M. Imada, A. Chutinan, and Masamitsu Mochizuki, "Polarization Mode Control of Two-Dimensional Photonic Crystal Laser by Unit Cell Structure Design," *Science,* vol. 293, pp. 1123-1125, 2001.

[57] X. Wu, A. Yamilov, X. Liu, S. Li, V. P. Dravid, R. P. H. Chang, and H. Cao, "Ultraviolet Photonic Crystal Laser," *Applied Physics Letters,* vol. 85, pp. 3657-3659, 2004.

[58] O. Sternberg, K. P. Stewart, Y. Hor, A. Bandyopadhyay, J. F. Federici, M. Bornefeld, Y.-L. Mathis, D. Sliwinski, K. D. Möller, and H. Grebel, "Square-Shaped Metal Screens in the IR to THz Spectral Region: Resonance Frequency,

Band Gap and Bandpass Filter Characteristics," *Journal of Applied Physics,* vol. 104, pp. 023103 2008.

[59] C.-C. Chen, "Transmission of Microwave through Perforated Flat Plates of Finite Thickness," *IEEE Transactions on Microwave Theory and Techniques,* vol. 21, pp. 1-6, 1973.

[60] R. Ulrich, *Modes of Propagation on an Open Periodic Waveguide for the Far Infrared* vol. XXIII. Brooklyn, NY: Polytechnic Press, 1974.